Flow Separation and Increased Drag Coefficient in Estuarine Channels With Curvature

Tong Bo[1,2] [ID] **and David K. Ralston[2]** [ID]

[1]MIT-WHOI Joint Program, Cambridge, MA, USA, [2]Applied Ocean Physics and Engineering Department, Woods Hole Oceanographic Institution, Woods Hole, MA, USA

Abstract Flow separation has been observed and studied in sinuous laboratory channels and natural meanders, but the effects of flow separation on along-channel drag are not well understood. Motivated by observations of large drag coefficients from a shallow, sinuous estuary, we built idealized numerical models representative of that system. We found that flow separation in tidal channels with curvature can create form drag that increases the total drag to more than twice that from bottom friction alone. In the momentum budget, the pressure gradient is balanced by the combined effects of bottom friction and form drag, which is calculated directly. The effective increase in total drag coefficient depends on two geometric parameters: dimensionless water depth and bend sharpness, quantified as the bend radius of curvature to channel width ratio. We introduce a theoretical boundary layer separation model to explain this parameter dependence and to predict flow separation and the increased drag. The drag coefficient can increase by a factor of 2–7 in "sharp" and "deep" sinuous channels where flow separation is most likely. Flow separation also enhances energy dissipation due to increased velocities in bends, resulting in greater loss of tidal energy and weakened stratification. Flow separation and the associated drag increase are expected to be more common in meanders of tidal channels than rivers where point bars that inhibit flow separation are more commonly found. The increased drag due to flow separation reduces tidal amplitude and affects velocity phasing along the estuary and could result in morphological feedbacks.

1. Introduction

1.1. Sinuous Tidal Channels

Rivers often have sinuous planforms (Langbein & Leopold, 1966). The natural processes that shape the sinuous form of river channels result from interactions between the fluid motion that carries sediment (e.g., along-channel flow and secondary circulation in a cross-sectional plane) and the erosion and deposition at river bed and bank (Langbein & Leopold, 1970; Seminara, 2006). In coastal systems where tides provide the dominant forcing, estuarine channels often exhibit similar sinuous geometry as river channels (Fagherazzi et al., 2004; Marani et al., 2002).

Channel curvature can cause secondary circulation in a lateral plane perpendicular to the flow direction, as a result of the local imbalance between the centrifugal acceleration and barotropic pressure gradient in the vertical (Thomson, 1877). Secondary circulation is predicted by the analytical solution presented by Rozovskii (1957) and Kalkwijk and Booij (1986), and observed in both rivers (e.g., Apmann, 1964) and tidal channel bends (e.g., Buijsman & Ridderinkhof, 2008; Chant, 2002; H. E. Seim & Gregg, 1997). This lateral circulation causes sediment transport across the channel and in turn provides feedbacks to meander morphology including erosion of outer bank, evolution of meander position, deposition at the inner bank, and growth of point bars. However, in curved estuarine channels, salinity stratification can suppress secondary circulation (e.g., H. E. Seim & Gregg, 1997) and the baroclinic pressure gradient can even reverse the sense of the lateral circulation compared to that expected for a river (e.g., Kranenburg et al., 2019). The reversed circulation due to baroclinic forcing may contribute to the absence of point bars in some tidal meanders, and the lack of bed-load transport in cohesive-bed tidal channels may also make it less likely for point bars to form (e.g., Jamieson et al., 2013).

Channel curvature can also cause flow separation of the along-channel velocity at the inside of bends, which is observed at sharp channel bends in both rivers (e.g., Ferguson et al., 2003) and tidal channels (e.g., Leeder & Bridges, 1975). The bend sharpness is customarily quantified as R/w, the ratio of bend radius of curvature

to channel width. Typical values of R/w are in the range of 1.5–4.3 for rivers (Leopold & Wolman, 1960) and 1.6–5 for tidal channels (Marani et al., 2002), and the bends where flow separation occurs tend to be sharper than average, for example, $R/w < 1.5$ (examined more below). Flow separation can significantly impact flow structure in curved channels and can increase along-channel drag (Blanckaert, 2015; James et al., 2001; Leopold, 1960), which will be discussed in the following section.

1.2. Increased Drag Coefficient in Sinuous Channels

In shallow coastal systems, bottom friction is a major source of drag, and it typically scales with physical roughness elements of the bed (bottom roughness z_0), whether grain size (Nikuradse, 1933) or bedforms (Grant & Madsen, 1982). Friction is customarily represented with quadratic velocity and a dimensionless drag coefficient C_D (see Equation 1). C_D can be related to z_0 and water depth by assuming a log-layer for near-bottom velocity. C_D is defined based on a reference velocity, usually taken at a fixed elevation (e.g., 1 m above the bed) or the depth-averaged velocity. A typical value for C_D of around 0.003–0.004 for shallow coastal and estuarine flows corresponds with a $z_0 = 0.002$ m for a reference velocity at 1 m above the bed or for depth-averaged flow for a water depth of 5 m. Other approaches to characterizing the effect of friction on open channel flow include Manning's n, the Darcy Weisbach f, and Chézy's C (James et al., 2001), but here we focus on the drag coefficient C_D.

In addition to bottom roughness, larger scale features can increase drag on the flow including coral reefs (e.g., Kunkel et al., 2006; Lentz et al., 2017; Rogers et al., 2018), vegetation (e.g., Kadlec, 1990; Monismith et al., 2019; Nepf, 1999), and form drag from topography (e.g., S. J. Warner & MacCready, 2014). This research will characterize a type of form drag, in particular on how channel meanders can increase the effective drag at larger scales. In this research, C_D is still defined based on quadratic velocity, but C_D quantifies the total drag instead of only bottom roughness. An example of form drag in a tidal flow was found for a headland in Puget Sound, where McCabe et al. (2006) and S. J. Warner and MacCready (2014) investigated the enhanced friction due to flow separation and internal wave generation.

Increased drag in sinuous channels compared with straight channels has been noted previously. In laboratory experiments with a sinuous channel, increased flow resistance and excess energy dissipation were observed around the bend (Leopold, 1960). In natural streams, meandering channels have been found to have Manning's n values as much as 30% greater than similar straight channels (Chow, 1959), and Arcement and Schneider (1989) suggested modifications to Manning's n to account for the increased drag in meandering rivers. Most of the examples of enhanced drag due to meanders are from rivers, but observations from a marsh also found increased surface slope in a sharply sinuous channel (Leopold et al., 1993), suggesting that the sharp bends may have contributed to the enhanced drag and increased Manning's n.

Several processes have been suggested as potentially contributing to enhanced drag with channel curvature, including dissipation in hydraulic jumps at high Froude number F_r (Leopold, 1960), extra bottom stress from lateral circulation (Chang, 1984), and form drag from flow separation (James et al., 2001). In tidal channels, F_r is usually relatively low, so hydraulic jumps are unlikely to occur. Lateral circulation, that is generated by the centrifugal acceleration of flow around bends and potential interactions with the salinity field, can enhance near-bed velocities and increase bottom stress and turbulent dissipation. Flow separation, in which streamlines of the along-channel flow detach from the channel bank and lead to a separation zone, has been observed in natural meanders, headlands and islands (e.g., Leeder & Bridges, 1975; Signell & Geyer, 1991; Wolanski et al., 1984). Flow separation creates a low-pressure zone behind the separation point and generates vortices from the boundary layer that are injected into the interior flow (Signell & Geyer, 1991). Flow separation in sinuous channels has been studied through laboratory measurements and observations. Lee eddies were observed in sinuous open channel experiments with relatively high mean velocity and strong curvature, causing the deformation of the free surface and restricting the flow to a narrower part of the cross section (Leopold, 1960). Inner bank separation and its influence on the flow structure were reported in sharp-bend flume experiments including Blanckaert (2011), Constantinescu et al. (2013), and Blanckaert (2015). In intertidal channels in the Solway Firth (Scotland), Leeder and Bridges (1975) noted that flow separation effectively decreased the width and increased the local velocity, and suggested that flow separation is to be expected in many natural systems. The formation of counter-rotating eddies near the apex of bends was reported by H. Seim et al. (2006) in the Satilla River estuary and noted to have similarities with flow

around headlands as in Signell and Geyer (1991). Flow separation in the lee of a bend and weak fluid recirculation in the separation zone were also observed in rivers, including the Embarras River (Frothingham & Rhoads, 2003) and the River Dean (Ferguson et al., 2003).

Although flow separation in sinuous channels has been widely observed, the influence of flow separation on resistance and drag remains mostly conceptual. James et al. (2001) investigated the drag increase associated with flow separation in laboratory sinuous channels and reported that vegetation can decrease drag compared to an unvegetated sinuous channel by reducing separation at sharp bend. James et al. (2001) showed the dependence of Manning's n on the curvature ratio R/w in unvegetated channels but with limited physical explanation. Blanckaert (2015) calculated the spatially distributed friction factor in a laboratory flume with bend-induced flow separation and noted the dependence of flow separation on H/w (depth to width ratio) and the curvature ratio R/w, but did not examine in detail the influence of these parameters on the drag. Leopold (1960) proposed that hydraulic jumps in the laboratory bend can explain the increased flow resistance and energy loss, but the flow in tidal channels rarely has sufficiently high F_r for this mechanism to apply.

1.3. Overview

In this project, we built idealized numerical models motivated by observations from the North River estuary (MA, USA) to explore the basic processes that lead to increased drag in sinuous channels. Previously, field studies were conducted in the North River estuary, a sinuous tidal channel through salt marsh that discharges into Massachusetts Bay (Kranenburg et al., 2019). The North River has relatively large tides (2–3.5 m range) and modest river discharge (typically <5 m³/s except for brief events of 10–30 m³/s), so stratification is weak and intermittent. The channel aspect ratio (channel width to depth, w/H) is about 10, and the bends are relatively sharp with the smallest R/w being 1.2. Measurements of velocity and pressure gradient in the North River resulted in a depth-averaged velocity drag coefficient C_D of 0.005–0.01 during ebb tide and 0.01–0.02 during flood tide (Kranenburg et al., 2017). However, typical values for estuaries with similar bottom roughness and water depth are in the range of 0.002–0.005 (e.g., Li et al., 2004). In the North River, local measurements of velocity and near-bed stress based on the turbulence spectra yielded a drag coefficient of 0.003 (Kranenburg et al., 2019), in this expected range and in sharp contrast to the C_D based on the pressure gradient that was greater by a factor of 2 to 7.

We examine the mechanisms by which flow separation in sharp sinuous channel bends can increase drag and energy dissipation using an idealized numerical model study scaled based on these observations. In section 2, we introduce the numerical model setup. Section 3 shows the effects of channel curvature on drag and tidal propagation, and investigates the increased drag and energy dissipation associated with flow separation. In section 4, we use numerical results to show the dependence of this increased drag coefficient on channel geometry. In section 5 we introduce a theoretical flow separation model to explain the parameter dependence and compare with our numerical results as well as previous research. In section 6, we discuss the influences of flow separation and the increased drag coefficient on sinuous channel dynamics and the broader application of the results, including comparison of rivers and tidal channels. Section 7 is a conclusion.

2. Model Setup

We applied the Regional Ocean Modeling System (ROMS) (Haidvogel et al., 2008; Shchepetkin & McWilliams, 2005; J. C. Warner et al., 2010) for the idealized sinuous estuary channel modeling. ROMS is a 3-D hydrostatic model based on the Reynolds-averaged Navier-Stokes (RANS) equations. The grid is structured, with high resolution in the sinuous region at the center of model domain and increasing grid spacing toward the open ocean boundaries and the upstream river boundary. A stretched, terrain-following coordinate is used with 16 layers uniformly distributed in the vertical direction. The sinuous estuary model (SIN1) has semidiurnal tides imposed onto the open ocean boundaries with a 12 h period, with a sinusoidal water level of 1 m amplitude (2 m tidal range) and velocity of 0.5 m/s. A constant river discharge of 5 m³/s is input at the upstream boundary, corresponding to a mean velocity of 1 cm/s in the upper channel and 0.5 cm/s in the sinuous channel near the estuary mouth. Salinity is 32 psu on the open ocean boundaries and 0 psu on the river boundary, and it is initialized as a linear decrease from the shelf into the estuary. Temperature is uniform throughout the entire domain. The model was run for a 20 day period, that is, 40 tidal cycles, to ensure that a quasi-steady state was reached. Model analysis was based on the last
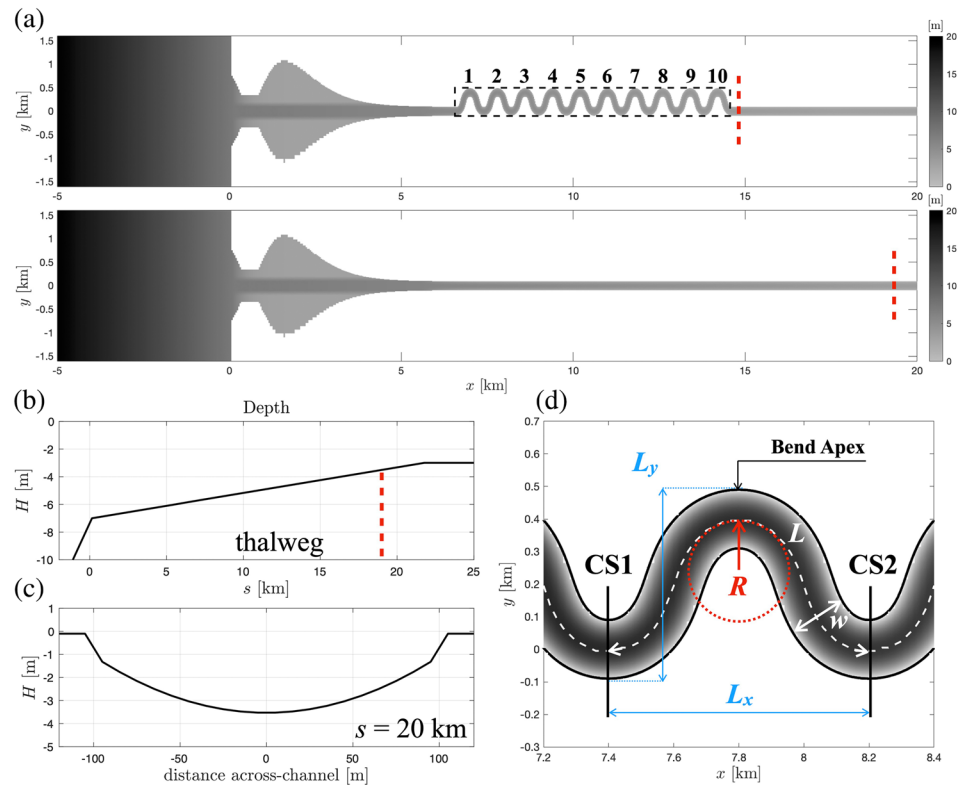
Figure 1. (a) Model bathymetry of the idealized sinuous and straight channel estuaries (SIN1 and STR1). Only the center parts of the model grids are shown. The estuary starts from $x = 0$, and $x < 0$ is the shelf. The sinuous region is marked by dashed black lines. Channel bends are numbered 1–10. (b) Depth of the channel thalweg as a function of along-channel distance s. (c) Cross-sectional bathymetry at $s = 20$ km, corresponding to the cross section denoted by the dashed red lines in subfigures (a) and (b). (d) Geometric parameters of channel Bend 2. L_x is the Cartesian length; L_y is the Cartesian width; L is the along-channel length. R is the minimum radius of curvature of the channel centerline along the bend. w is the channel width. Black lines mark the position of cross sections (CS1, CS2) used in the following model analysis.

two tidal cycles. The generic length-scale (GLS) mixing scheme is used for the vertical turbulent mixing (Umlauf & Burchard, 2003; Warner et al., 2005) and the horizontal mixing coefficient K_H is set to 0.01 m^2/s. Bottom roughness z_0 is 0.002 m, a typical value for a bed with ripples (Grant & Madsen, 1982). A constant and uniform z_0 is used to avoid introducing other sources of variability that affect the drag, but we note that natural channels can have spatially and temporally variable physical roughness.

The shelf is 40 km long and 14 km wide, with depth linearly decreasing from 100 to 7 m toward the coast. A narrow tidal inlet (700 m wide) is located at the estuary mouth, followed by a lagoon with a channel (400 m wide) in the middle and shallow flats on the side. The channel exponentially converges landward (e.g., Langbein, 1963) until 6.5 km into the estuary, and after that the channel is uniform width $w = 200$ m, with 20 grid cells across the channel. A sensitivity test was also conducted with double the grid resolution and the results were the same. The sinuous region is located between 6.5 and 19 km, and the total along-channel length is approximately 40 km. Channel thalweg depth linearly decreases from 7 m at the mouth to 3 m at 22 km, with a slope of ~0.18 m/km, and the thalweg depth is a uniform 3 m from 22 km to the landward boundary (Figure 1b). The channel has a parabolic cross-sectional profile (e.g., Smith, 1982) with a minimum depth of 1.5 m to ensure that the bed does not emerge at low tide (Figure 1c). The sinuous channel shape is created following the form of sine-generated functions (Langbein & Leopold, 1970), and the mathematical expression is shown in Appendix A. The sinuous region is composed of 10 continuous 144° bends, numbered in Figure 1a, where we are focusing on just half the bends to limit redundancy. The minimum radius of curvature of the channel centerline is 164 m at the bend apex. The Cartesian length of each channel bend is 800 m and the Cartesian width is 600 m; the along-channel length of each bend is 1,240 m (Figure 1d).

Table 1
Parameters of All the Models

Model	R (m)	h (m)	H (m)	w (m)	L (m)	R/w	H/w	H/L
STR1	—	3–7	2–6	200	—	—	0.01–0.03	—
STR2	—	7–12	6–11	200	—	—	0.03–0.06	—
SIN1	164	3–7	2–6	200	1240	0.82	0.01–0.03	0.002–0.005
SIN2	164	7–12	6–11	200	1240	0.82	0.03–0.06	0.005–0.009
SIN3	46	3–7	3–5	60	540	0.77	0.05–0.08	0.005–0.009
SIN4	270	3–7	3–6	200	1550	1.35	0.01–0.03	0.002–0.004
SIN5	185	3–7	3–6	200	1080	0.93	0.01–0.03	0.003–0.006
SIN6	185	3–7	3–6	160	1080	1.12	0.02–0.04	0.003–0.006
SIN7	185	3–7	3–6	120	1080	1.54	0.03–0.05	0.003–0.006
SIN8	185	3–7	3–6	140	1080	1.32	0.02–0.04	0.003–0.006

Note. STR1 and STR2 are straight channel models, and SIN1–SIN8 are sinuous channel models. R is the minimum radius of curvature. h is the thalweg depth. H is the cross-sectionally averaged water depth, which varies with distance along the channel and tidal water level. L is the along-channel length of each bend.

A straight channel model (STR1) is used as a comparison of the sinuous channel model (SIN1). The boundary conditions, channel width, depth, bottom slope and lateral bathymetric profile are exactly the same in the two models and the only difference lies in the channel planform. The total along-channel length is also the same to make the total volume of the two estuaries identical. The grid is adjusted near the river boundary so that the straight model domain is longer than the sinuous model to ensure the same along-channel length, but the grid at the center of the domain (i.e., the high-resolution region used for analysis) is the same.

Additional model grids with different sinuous channel shapes are used to explore parameter space (Table 1), but the overall structure and model settings are similar for the other cases. The tidal range is 2 m for all the models, consistent with the neap tide condition on the North River estuary. A 3.2 m tidal range representative of spring tides was also examined and produced similar results. SIN1 and STR1 are the pair of sinuous and straight channels introduced above. SIN2 and STR2 are another pair of sinuous and straight channels with the same channel shape as SIN1 and STR1 but greater depth. SIN3–SIN8 are other sinuous channel cases that are also created using a series of sine-generated functions (Langbein & Leopold, 1970). Details are given in Appendix A, and representative channel shapes are shown in Figure A1. The results and analysis in section 3 are based on models SIN1 and STR1. Sections 4 and 5 draw on results from all the models in Table 1. The channel aspect ratio among the model cases varies between 10 and 60, which covers a wide range of salt marshes, tidal flats and rivers, and the R/w (bend sharpness) ranges between 0.7 and 1.6. The numerical experiments and the field study that inspired them focus on channel bends that are relatively sharp for rivers and tidal meanders (Leopold & Wolman, 1960; Marani et al., 2002), but they are within the range commonly found in nature (e.g., Marani et al., 2002; Nanson, 2010; Schnauder & Sukhodolov, 2012).

3. Numerical Model Results

In this section, we analyze model results and explore the underlying physics that cause the increased drag in meanders. In section 3.1, we compare drag coefficients between the sinuous (SIN1) and straight (STR1) estuary models. In section 3.2, we examine the effects of the increased drag with channel curvature on tides and stratification. In section 3.3, we characterize flow separation and secondary circulation, and calculate the form drag. In section 3.4, we calculate the energy budget and show how flow separation increases energy dissipation.

3.1. Increased Drag Coefficient in Meanders

It is customary to write drag force as

$$\tau = \rho C_D u_r |u_r|, \tag{1}$$

where τ is the total drag force, including bottom stress and other sources of drag. ρ is density, C_D is the drag coefficient and u_r is a reference velocity, often taken as the depth-averaged velocity or the velocity at a fixed elevation above the bottom. Here we take the reference velocity u_r as the cross-sectionally averaged streamwise velocity U.
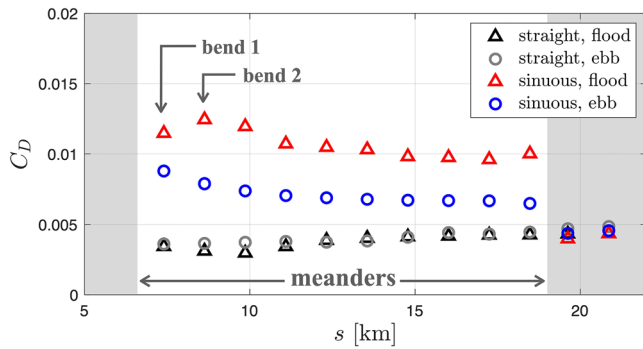
Figure 2. Drag coefficient as a function of along-channel distance. C_D is averaged over flood and ebb tide separately in both the straight and sinuous models. The black triangles and gray circles represent flood and ebb tide, respectively, in the straight model; the red triangles and blue circles represent flood and ebb tide in the sinuous model. The white background shows the range of meanders (the sinuous region), and the arrows mark the first two bends as a representative. The first 10 points represent the 10 bends in the sinuous region; the last two points show the drag coefficient at a similar spacing outside the sinuous region.

The drag coefficient is used to represent resistance in the along-channel momentum equation

$$\frac{\partial U}{\partial t} + U\frac{\partial U}{\partial s} = -g\frac{\partial \eta}{\partial s} - \frac{1}{2}\beta g\frac{\partial S}{\partial s}H - C_D\frac{U|U|}{H}, \qquad (2)$$

where η and H are the laterally averaged water level and water depth, and S is the cross-sectionally averaged salinity. β is the haline contraction coefficient. s is the along-channel coordinate. Local (depth-averaged) velocity, water level, salinity are often all that can be measured in field observations, but here we used the cross-sectional average of all the properties because of the large lateral variations in these quantities in the sinuous channel case. The advection term associated with cross-stream velocity is neglected in cross-sectionally averaged momentum budget because it is small. We can calculate an effective C_D that satisfies the momentum budget

$$C_D = \left(\frac{\partial U}{\partial t} + g\frac{\partial \eta}{\partial s} + \frac{1}{2}\beta g\frac{\partial S}{\partial s}H + U\frac{\partial U}{\partial s} \right) \Big/ \left(\frac{-U|U|}{H} \right). \qquad (3)$$

We calculated the effective drag coefficient across the bend between sections CS1 and CS2 over a tidal cycle using (3). Only the bend-scale drag coefficient is calculated because form drag is usually defined as a spatial integral over the topography of interest (McCabe et al., 2006). The drag coefficient in the straight model is evaluated at locations with same along-channel distance. Data points near slack water are removed to avoid very small values in the denominator of (3). In both models, the water level gradient is the dominant term, and the unsteady, advective, and baroclinic terms are at least an order of magnitude smaller.

Model results show that the drag coefficient in the sinuous estuary is two to four times larger than the straight estuary, for example, 0.006–0.015 compared to 0.003–0.004. The models are identical except for the channel meanders, suggesting that this increase in drag by a factor of 2–4 is associated with the sinuous planform. C_D is averaged over flood and ebb tide separately in both models (Figure 2). In the straight model, C_D is slightly larger during ebb tide than flood tide, but differences are small. In the sinuous channel, the drag coefficient is larger during flood tides than ebb tides. The drag coefficient also shows temporal fluctuations during flood tides due to instability in the flow field, so the maximum C_D (e.g., ∼0.015 in Bends 1–3) is larger than the temporal average C_D (e.g., ∼0.012 in Bends 1–3) in Figure 2. Both the magnitude of the drag coefficient in the sinuous channel and the flood-ebb asymmetry are broadly consistent with field observations from the North River, on which the model grid was scaled (Kranenburg et al., 2017).

In the sinuous region, the drag coefficient is significantly larger than that of the straight model, while outside the sinuous region the drag coefficient decreases and is consistent with the straight model. The drag coefficient also has different along-channel trends in the two models. The drag coefficient in the straight model increases landward, while in the sinuous model C_D has a decreasing trend. These opposite behaviors are related to the different depth dependence of C_D in the two models and will be explained in section 4. As a result, difference between the sinuous and straight models is greatest in the seaward bends, and we have focused the subsequent analyses on Bend 2.

3.2. Along-Channel Change of Tides and Stratification

In shallow estuaries or inlet systems, the drag directly affects tidal propagation, including tidal amplitude decay and phase lag with distance along the estuary (e.g., Aubrey & Speer, 1985). The increased drag in tidal meanders can therefore have important influences on the water level change in estuaries, which impacts coastal flooding and marsh resilience. Harmonic analysis is employed to examine the influences of meanders on tidal elevation. The numerical system is forced by a 12 h semidiurnal tide, so in the harmonic analysis, M2 (12 h) tide and M4 (6 h) and M6 (4 h) overtides are selected as three major tidal components for least squares fitting.

The amplitude and phase of the dominant M2 tide is shown in Figure 3. In the straight model, the amplitude of M2 tide decays as it propagates into the estuary until being reflected near the upstream river boundary. The decay rate is ∼0.024 m/km, which is mainly attributed to frictional dissipation. The sinuous model shows a
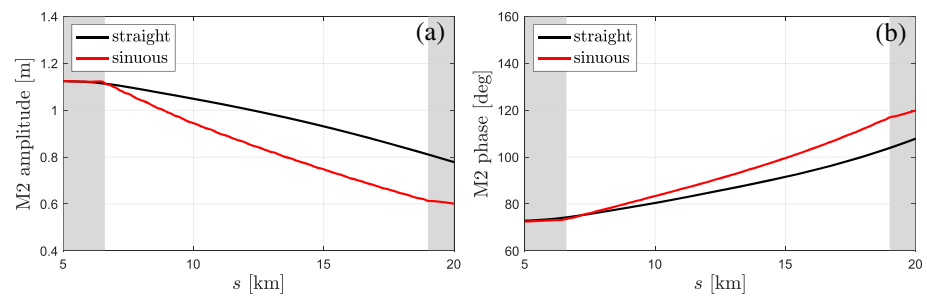
Figure 3. (a) M2 tidal amplitude along the channel. (b) M2 tidal phase along the channel. Red lines represent the sinuous model, and black lines represent the straight model. The white background shows the range of the sinuous region.

faster tidal amplitude decay (~0.040 m/km) than the straight model, which indicates a greater energy loss (details discussed in section 3.4). Also, the M2 tidal phase lag is greater in the sinuous channel than the straight channel, as is expected from the increased effective drag (Aubrey & Speer, 1985).

Comparison of tidal elevation in the two models demonstrates that meanders can affect tidal water levels in the landward parts of the estuary. Meanders also can impact the growth of overtides and tidal asymmetries. The ratio of amplitudes M4/M2 is similar in the two models but M6/M2 is larger in the sinuous model than the straight model by almost a factor of 2, indicating greater nonlinearity with the sinuous channel.

The cross-sectionally averaged velocity U is less in the sinuous channel than the straight, which is in agreement with the tidal amplitude decay in Figure 3. Decreased tidal amplitude indicates smaller estuary volume change associated with tidal fluctuations and, as a result, smaller volumetric flux and weaker cross-sectional average current. However, despite the weaker cross-sectionally averaged velocity, the maximum local velocities in the sinuous channel exceed those in the straight channel by up to 30%. This result suggests stronger lateral variations in the velocity field because of channel bends.

Differences in stratification are also apparent between the sinuous and straight channel cases. In both cases, the tidally averaged ΔS (difference between surface and bottom salinity) is less than 6 psu, relatively weak stratification that is consistent with the strong tidal currents and small river discharge. However, the sinuous model has a smaller tidally averaged ΔS than the straight channel, indicating weaker stratification due to the existence of channel bends. The mechanism of how sinuous channels decrease stratification is still unclear, and could be related to secondary circulation in the bend or flow separation near the bend apex.

3.3. Flow Separation and Form Drag

Flow separation can generate recirculating eddies near the inner bank and produce a "dead zone" or "separation zone" in the lee of channel bends (e.g., Blanckaert, 2011; Ferguson et al., 2003; Rozovskii, 1957), which narrows the effective flow width and increases the local velocity (Leeder & Bridges, 1975; Leopold, 1960). Although outer bank separation is also observed in some channel bends (e.g., Blanckaert et al., 2013), the present research focuses on separation at the inner bank.

Flow separation is seen in model results at both maximum flood and maximum ebb, and here we take flood tide as an example (Figure 4a). The lateral profile of velocity becomes deflected away from the inner bank and the separation zone grows from near the bend apex toward the lee of bend. The boundary of the separation zone is represented by the deflection points in the velocity profiles. Streamlines at maximum flood are also displayed in Figure 4a, with a recirculating eddy in the lee of the channel bend. Free surface deformation is observed in the lee of bend, which is related to the formation of recirculating lee eddies (Leopold, 1960). The water level field can be regarded as the depth-averaged barotropic pressure field. A sudden pressure drop occurs near the boundary of the separation zone and a low pressure zone is located downstream of the bend. This pressure drop creates an extra "form drag" or "pressure drag," that increases the drag coefficient. Flow separation also increases instability in the velocity field, which is reflected in temporal fluctuations in C_D.

The separation zone decreases the main flow width and consequently increases the main flow velocity outside the separation zone. We define an effective width for the main flow due to the expansion of flow separation into the channel, as illustrated in Figure 4b. The effective main flow region is defined by $\overline{u} > 0.5U$, with $\overline{u}$ being the local depth-averaged streamwise velocity and U being the cross-sectionally averaged
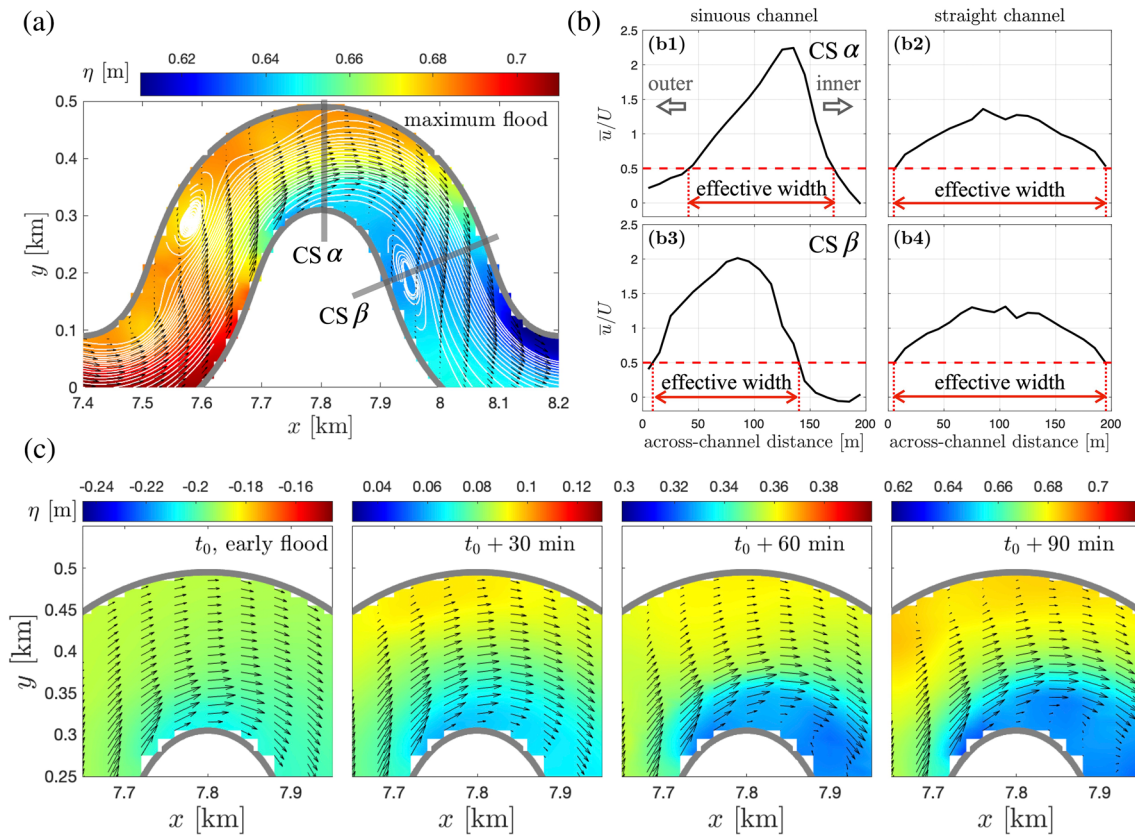
Figure 4. (a) Water level, streamlines, and velocity field of channel Bend 2 at maximum flood tide. White lines show streamlines, including the main flow and the recirculating eddy in the lee of Bend 2. Black arrows show the depth-averaged velocity. Gray lines represent the river banks. (b) Lateral profile of streamwise velocity scaled by local cross-sectional average velocity at two cross sections in the sinuous channel and the same along-channel distance locations in the straight channel. The inner bank is on the right side of the graph. Effective channel width is defined as the lateral length of where $\bar{u} > 0.5U$, in which $\bar{u}$ is the local depth-averaged streamwise velocity and U is the cross-sectionally averaged streamwise velocity. (b1) and (b3) correspond to cross sections CSα and CSβ in Panel (a), respectively. (b2) and (b4) show locations with the same along-channel distance in the straight channel. (c) Evolution of flow field near the bend apex, with snapshots of four different times during early flood tide. The colormap shows the water level. The range of the colormap varies as water level grows during early flood, but the span of the colormap is the same in all the small panels. t_0 is early flood tide, and $t_0 + 90$ min is maximum flood tide.

streamwise velocity. The effective width is decreased by ~20–30% in the sinuous channel because of flow separation, while in the straight channel, the effective width is equal to the channel width. Along-channel momentum is more concentrated into a narrower main flow region in the sinuous channel and maximum velocity is intensified as a result of effective width decrease, which explains why the maximum velocity is greater in the sinuous model despite lower cross-sectional average velocities than the straight model (section 3.2).

The evolution of velocity field during early flood tide illustrates the occurrence of flow separation (Figure 4c). During early flood prior to flow separation, flow is attached to the inner bank with the maximum streamwise velocity near the inside of the bend. This is common in flat bottom channel flow in the laboratory (e.g., Blanckaert, 2015) and natural meanders without a point bar (e.g., Jamieson et al., 2013; Kranenburg et al., 2019). Flow near the inner bank is decelerated after passing the bend apex because of the adverse pressure gradient set by channel curvature. As the tidal current grows, this adverse pressure gradient is strengthened and velocity near the inner bank keeps decreasing until the main flow detaches from the inner bank and flow separation occurs. The maximum velocity increases as the effective width of the main flow decreases, with the velocity maximum separated from the inner bank and shifted toward the center of the channel (also see Kranenburg et al., 2019 Figure 7). Flow near the inner bank can slow to 0 or reverse as the flow separation evolves, which leads to the formation of recirculating eddies.

Lateral water level variations are also increased as the tidal current grows (Figure 4c). The lateral barotropic pressure gradient set by the water level combined with the centrifugal acceleration can generate the
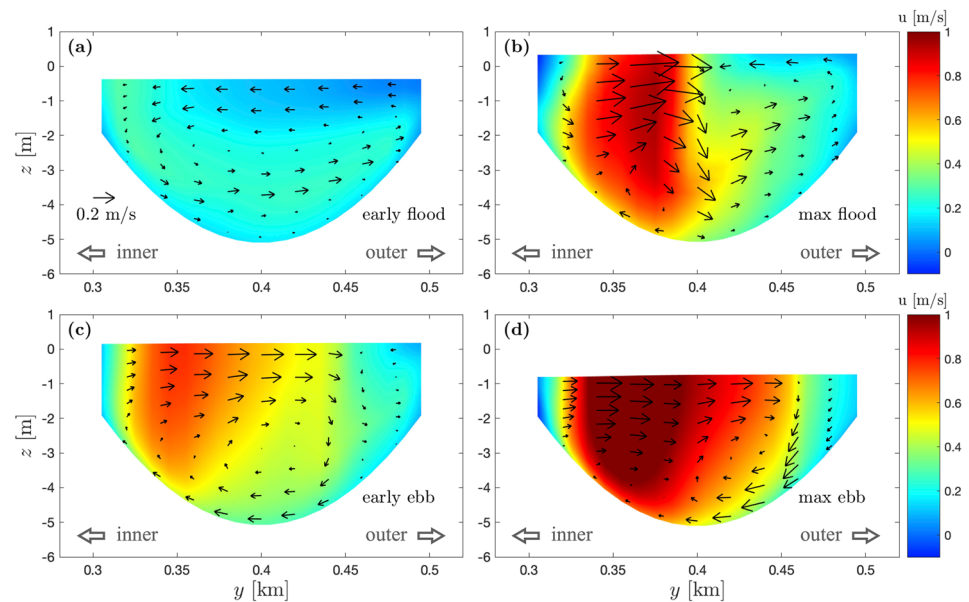
Figure 5. Along-channel velocity contours and secondary circulation structure in the cross section at the apex of Bend 2. (a) Early flood tide; (b) maximum flood tide; (c) early ebb tide; (d) maximum ebb tide. The colormaps show the along-channel velocity. Note that the positive direction is landward for flood tide and seaward for ebb tide. Black arrows show the lateral and vertical velocity. The inner bank is on the left side, and outer bank is on the right side in all panels.

"normal" secondary circulation for homogeneous flow around a bend, with cross-channel velocity toward the outside of the bend at the surface and toward the inner bank near the bottom. Normal secondary circulation is observed at ebb tide with a small counter-rotating circulation cell near the outer bank (Figure 5c), similar to Blanckaert and De Vriend (2004) and Blanckaert (2011). At maximum ebb tide, the normal secondary circulation cell has shifted slightly away from the inner bank due to the flow separation with reversed along-channel flow occurring there (Figure 5d).

Lateral salinity differences can also affect the lateral circulation, potentially reversing it from the normal homogeneous secondary circulation (e.g., Kranenburg et al., 2019). The reversed circulation is observed during early flood tide (Figure 5a) when differential advection with relatively larger velocity near the inner bank (Figure 4c) brings higher salinity to create a cross-channel density gradient, as is found in Kranenburg et al.'s (2019) Figure 9. Lateral circulation cells become more complex at maximum flood tide when flow separation occurs near the inner bank (Figure 5b). A normal secondary circulation cell grows driven by the strong along-channel vertical shear and the lateral water level gradient near the boundary of the flow separation zone (Figure 4c), and the reversed lateral circulation cell that was predominant during the early flood is pushed toward the outer bank.

Secondary circulation increases momentum loss both through the cross-channel component of the bed shear stress and by redistributing the along-channel momentum (Blanckaert & de Vriend, 2003). The magnitude of cross-channel bottom velocity is about 0.1 m/s, and the along-channel bottom velocity is typically 0.3–0.5 m/s. Thus, based on the quadratic drag formulation the total bottom stress including the cross-channel component is ∼10% greater than for the along-channel component alone. The effects of secondary circulation redistributing along-channel momentum are difficult to isolate because flow separation also redistributes the along-channel momentum by restricting the main flow to a narrower region. During early flood tide the reversed lateral circulation tends to bring higher momentum toward the inner bank (Figure 5a), whereas the flow separation at max flood tide detaches the higher velocity zone from the inner bank and shifts it outward (Figure 5b). The dominance of the flow separation on lateral redistribution around max flood suggests that flow separation plays a more important role than secondary circulation in the sinuous channel cases. These sinuous model cases have relatively sharp bends where flow separation is favored, and the relative influence of secondary circulation on the drag may be greater for channels with smoother bends.
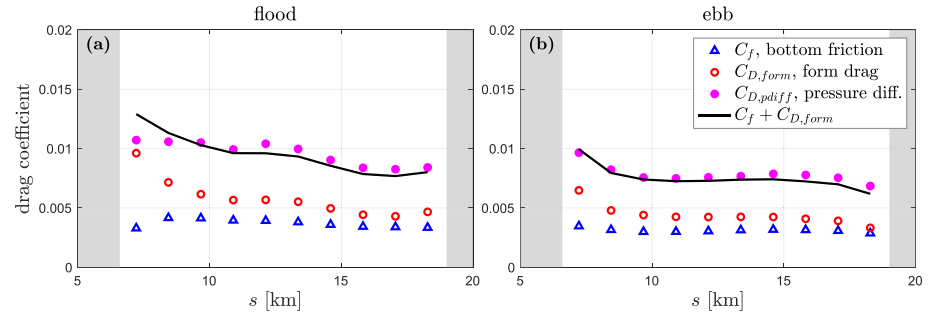
Figure 6. Drag coefficients corresponding to different terms of momentum loss. (a) Maximum flood tide. (b) Maximum ebb tide. Magenta dots represent the pressure difference around each bend; red circles represent the form drag; blue triangles represent bottom friction. Black lines are the sum of bottom friction and form drag, that is, the total drag. All the terms are calculated or integrated over channel bend scale and converted into corresponding drag coefficients. The white background shows the range of the sinuous region.

To quantify the form drag contribution directly, we write the integral form of the momentum equation (McCabe et al., 2006) over each bend as

$$\frac{\partial}{\partial t} \int_V \rho_0 u \, dV + \int_{A_{CS1+CS2}} \rho_0 u \vec{u} \cdot \vec{n} \, dA = \int_{A_{CS1}} p \, dA - \int_{A_{CS2}} p \, dA + \int_{A_w + A_b} p \xi_x \, dA + \int_{A_b} \tau_{bx} \, dA, \tag{4}$$

where ξ_x corresponds to the projection in x direction. A_{CS1} and A_{CS2} represent the cross-sectional areas at each end of the control volume; A_w and A_b represent the areas of the vertical sidewalls and channel bed. The density ρ_0 is homogeneous and stationary based on the Boussinesq approximation. The momentum budget is calculated at maximum flood and maximum ebb. The unsteady and advection terms on the left side of (4) are small, so the momentum budget in x direction results primarily from the pressure difference between the two cross section ends (first two terms on the right side of (4)), the form drag (third term), and the bottom friction (last term), as there is no friction on the surface or sidewalls of our model. Baroclinic effects are also small (section 3.1) so only the barotropic pressure is included in this calculation.

In the straight model, the pressure difference between the ends of the control volume is balanced by bottom friction, and there is no form drag due to the channel geometry (Appendix B). The decreasing thalweg depth along the channel also creates a large pressure force between the ends of the control volume that is balanced by the bottom slope, and we have removed this bottom-slope effect in calculating the momentum budget to focus on the pressure force and form drag associated with water level (Appendix B). In the sinuous model, the right-side terms in (4) are calculated over each bend and converted into corresponding drag coefficients based on the cross-sectional average velocity (Figure 6). $C_{D,pdiff}$, $C_{D,form}$ and C_f correspond to the pressure difference, form drag and bottom friction, respectively. The drag in Figure 6 is calculated slightly differently from that in Figure 2—Figure 2 shows the temporal average, while Figure 6 uses snapshots at maximum flood and maximum ebb—but the results are consistent. The bottom friction in the sinuous channel is similar to the straight channel, for example, $C_f \sim 0.003$–0.004. The pressure difference (total drag) is a factor of ~ 2–3 larger than bottom friction in the sinuous channel, indicating that there is another source of momentum loss, that is, the form drag associated with flow separation. Integration of the sidewall and channel bed pressure (projected in the x direction) directly represents the effect of the form drag on the momentum budget, and shows that it is up to a factor of 2 larger than bottom friction, and the momentum budget closes only when the pressure difference is balanced by the combination of bottom friction and form drag.

3.4. Energy Dissipation

Flow separation not only causes an extra momentum loss by creating form drag, but also leads to a larger energy dissipation in the sinuous channel. The integral form of the energy equation (Gill, 1982; Zhong & Li, 2006) for horizontal velocities is

$$\int_{A_{CS}} \left(p + \rho_0 \frac{u^2 + v^2}{2} \right) \vec{u} \cdot \vec{n} \, dA = - \int_{A_b} \vec{u}_b \cdot \vec{\tau}_b \, dA - \int_V \rho_0 K_V \left[\left(\frac{\partial u}{\partial z} \right)^2 + \left(\frac{\partial v}{\partial z} \right)^2 \right] dV$$

$$- \int_V \rho_0 K_H \left[\left(\frac{\partial u}{\partial x} \right)^2 + \left(\frac{\partial u}{\partial y} \right)^2 + \left(\frac{\partial v}{\partial x} \right)^2 + \left(\frac{\partial v}{\partial y} \right)^2 \right] dV. \tag{5}$$
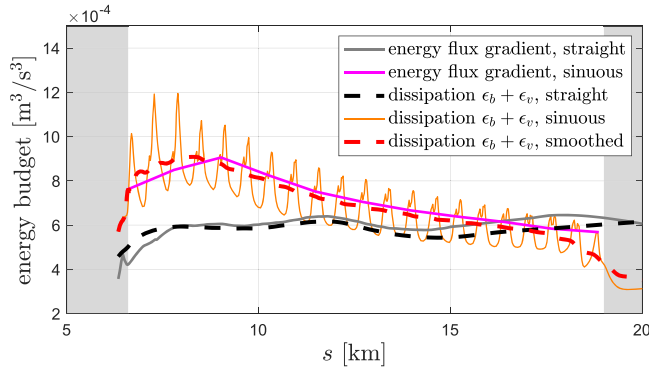
Figure 7. Terms in the energy budget in the sinuous and straight models as a function of along-channel distance. Solid gray and solid magenta lines represent the energy flux gradient in the straight channel and sinuous channel (evaluated at bend scale). Solid orange line: bottom dissipation ϵ_b and vertical dissipation ϵ_v in the sinuous channel. Dashed red line: $\epsilon_b + \epsilon_v$ in the sinuous channel smoothed (using a moving average) over the bend scale. Dashed black line: $\epsilon_b + \epsilon_v$ in the straight channel. The white background shows the range of the sinuous region.

The left side is the net energy flux and the unsteady term is neglected as we have focused on the tidally averaged energy balance. The right side is energy dissipation, which is composed of three parts: energy loss due to bottom shear stress ϵ_b (the surface and sidewall stress are 0 in our models), vertical turbulent dissipation ϵ_v (the vertical viscosity K_V is set by the turbulence closure) and horizontal dissipation ϵ_h (the horizontal viscosity $K_H = 0.01$ m^2/s). Energy flux and the three dissipation terms in the energy budget are calculated along the channel and converted to depth-integrated and laterally averaged results (Figure 7).

In both the straight and sinuous models, the energy flux loss is generally balanced by the calculated total dissipation, which demonstrates that the energy budget closes in the models and numerical dissipation is negligible. Comparing the two models, we found that there is a larger energy loss in the sinuous model (Figure 7), which is consistent with the greater rate of decrease in tidal amplitude in section 3.2. The maximum dissipation values in the sinuous model, and therefore maximum energy loss rates, occur near the bend apexes.

The larger energy loss induced by meanders is caused by both increased dissipation associated with bed stress and enhanced vertical dissipation by turbulence. The bottom stress dissipation is larger in the sinuous model than the straight model, even though bottom stresses are similar in the two models (section 3.3). This can be explained by the decreased effective channel width due to flow separation near the bend apex, which accelerates the main flow because of continuity. Bottom dissipation can be estimated as

$$\epsilon_b = \tau_b u_b \sim \rho C_f u_r^2 u_b, \tag{6}$$

where τ_b is the bottom stress, u_b is the bottom velocity and u_r is a reference velocity associated with the bottom friction coefficient C_f. The cubic dependence of dissipation on velocity, together with the greater velocity near the channel center due to flow separation, leads to a larger laterally averaged bottom stress dissipation in the sinuous channel.

The vertical turbulent dissipation depends on the vertical shear and vertical turbulent viscosity. Numerical results show that the vertical profile of streamwise velocity is more uniform in the sinuous model than the straight channel, so there is less streamwise vertical shear. However, the vertical turbulent viscosity is increased in the sinuous model as a result of weaker stratification compared with the straight channel. The source of this reduction in stratification and enhanced turbulence is still unclear, and it could be associated with the accelerated streamwise velocities or the stronger secondary circulation. For comparison, Nidzieko et al. (2009) found in a curved estuary channel that the destratification was caused by turbulent motions rather than an overturning produced by lateral circulation. As with bottom dissipation, the vertical turbulent dissipation scales with velocity cubed, so the increased turbulent dissipation in meanders also relates to the decreased effective channel width and velocity acceleration because of flow separation.

Secondary circulation increases both bottom shear stress and internal friction by introducing in stronger lateral velocity and lateral shear (Chang, 1984) and thus leads to additional energy loss. However, the extra dissipation contributed by secondary circulation (i.e., the bottom dissipation associated with lateral bottom shear stress and the turbulent dissipation created by the vertical shear of cross-channel velocity) is less than 30% compared to the total dissipation in the straight channel (see supporting information for details).

Horizontal dissipation also could contribute to the enhanced energy dissipation in the sinuous channel case. High vorticity fluid is generated near the inner bank due to the velocity shear set by the shallower bathymetry near the edges of the channel, and the high vorticity fluid can be injected into the center of the channel by flow separation, potentially increasing horizontal dissipation (e.g., Figures 9a and 9c). Signell and Geyer (1991) discussed similar processes of eddy formation around headlands and injection of high vorticity fluid from the boundary layer into the interior flow. However, although we observed greater horizontal dissipation in the sinuous channel than the straight channel, that term is still 2 orders of magnitude smaller than the bottom stress and vertical turbulent dissipation terms.
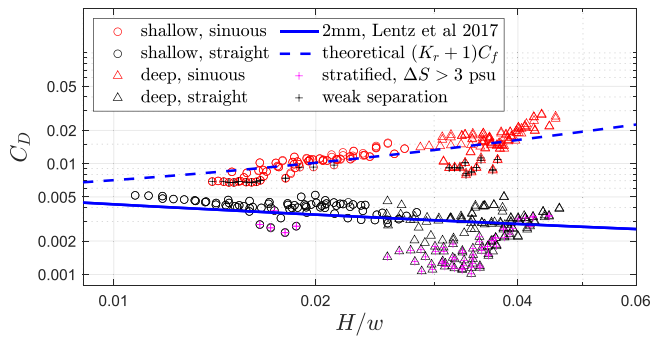
Figure 8. The drag coefficient as a function of H/w, with H being the laterally averaged water depth. Red circles: shallow sinuous model (SIN1); red triangles: deep sinuous model (SIN2); black circles: shallow straight model (STR1); black triangles: deep straight model (STR2). The solid blue line shows the C_D predicted by (7) with $z_0 = 2$ mm. The dashed blue line shows the C_D predicted by (13) in section 5. The two shallow channel models (SIN1 and STR1) were the original models employed in section 3, and the two deep channel models (SIN2 and STR2) have the same channel shape as the shallow models and a depth of 7–12 m. In the straight model, stratified cases during ebb tide ($\Delta S > 3$) are filled with magenta plus signs. In the sinuous model, weak flow separation cases (effective width $>0.9w$) are filled with black plus signs.

Previous investigations of the energy loss induced by sinuous channels proposed that the major sources of energy loss included increased bed friction from secondary circulation, increased turbulence induced by secondary circulation and turbulence in eddies associated with flow separation (e.g., James et al., 2001). However, our research suggests that the momentum redistribution caused by flow separation, that is, decreased effective width and increased local streamwise velocity, is an important source of energy loss. These results are particularly relevant to tidal channels, which are shallower than most of the laboratory channels based on aspect ratio. For shallow systems, dissipation is primarily related to the bottom stress and vertical shear even though there is strong horizontal variation in velocity induced by the complex geometry.

4. Parameter Dependence of the Drag Coefficient

4.1. Parameter Dependence on Water Depth

For turbulent open channel flow with small roughness compared to the water depth, Lentz et al. (2017) proposed an estimate for the drag coefficient based on the depth-averaged velocity

$$C_D \approx \kappa^2 \left[\log\left(\frac{H}{z_0}\right) + (\Pi - 1) \right]^{-2}, \tag{7}$$

in which $\kappa = 0.41$ is the von Kármán constant. z_0 is the bottom roughness and H is the water depth. Π is Cole's wake strength and $\Pi \approx 0.2$ for turbulent open channel flow (Nezu, 1993). In this formulation, C_D decreases as water depth increases, because velocity profile becomes less sheared in the upper water column with greater flow depth.

Results from the straight channel models (STR1 and STR2) show a decreasing trend with depth that is consistent with the theoretical C_D in (7), as Figure 8 shows. The simulation results do not exactly match the theoretical result because we have parabolic channels instead of flat bottom channels, and the velocity profile can be altered by stratification. In the straight channel, the estuary is more stratified during ebb tide and these stratified periods ($\Delta S > 3$) have a smaller drag coefficient than predicted by the formula, as are marked in Figure 8. The dependence of C_D in the straight channel is only on water depth H but not channel width w. Although H is nondimensionalized by w to follow the convention of research on meanders, w is a constant in the models employed in Figure 8, so channel width does not affect the decreasing trend in the straight models.

In the sinuous channel models (SIN1 and SIN2), C_D increases with the water depth scaled by channel width, which indicates a different dominant mechanism in exerting drag from the straight channel. Calculations of C_D are based on 1 h averages to filter out fluctuations caused by instability associated with flow separation. As is discussed in section 3.3, flow separation is the major source of drag instead of bed friction. Therefore, C_D in sinuous channels has the opposite depth relation because flow separation is stronger in deeper water where it is less inhibited by bottom friction, which thus leads to a larger momentum loss and a larger C_D. Some weak flow separation cases are marked out in Figure 8, identified as bends where the effective width $>0.9w$ (w is channel width). These weak separation cases have relatively small drag coefficients, and occur only during ebb tide. The causes for this weak separation are still unclear, and may depend on inhibition by the shallow bathymetry near the inner bank, greater stratification, or the secondary circulation.

The dependence on water depth explains the flood-ebb asymmetry in C_D (section 3.1). Water is deeper during flood tide because of the phase lag between water level and velocity, and as a result, C_D is larger during flood tide (section 3.1). The increasing or decreasing trend of C_D along the channel (Figure 2) is also related to its dependence on water depth. The channel becomes shallower in the landward direction with a slope of ~ 0.18 m/km (section 2). In the straight channel, C_D increases as water depth decreases (Figure 8), so C_D increases landward in Figure 2. On the contrary, in the sinuous channel where flow separation creates form drag, C_D decreases as water depth decreases (Figure 8) and as a result C_D decreases landward in Figure 2.

Unlike in straight channels in which C_D only depends on H, C_D in sinuous channels depends on both H and w. Blanckaert (2015) found that the width of flow separation zone primarily scales with the water
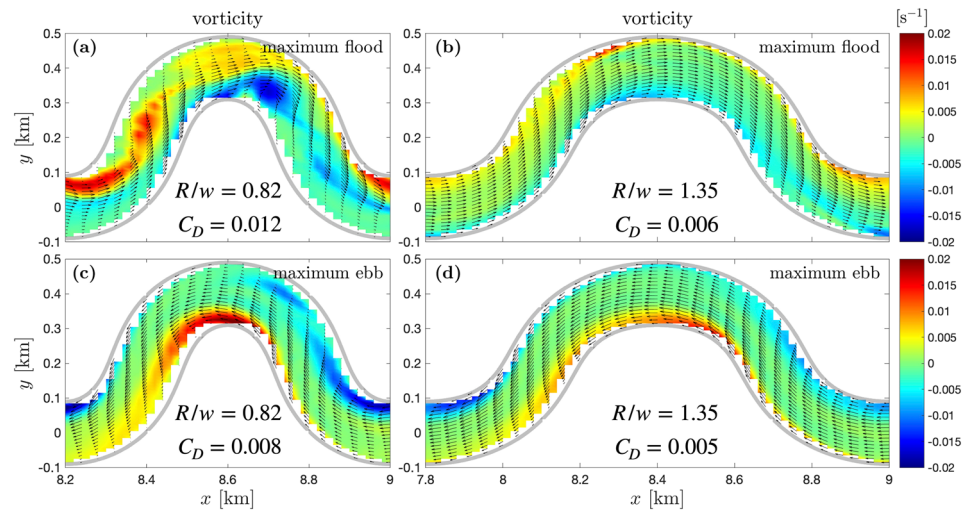
Figure 9. Vorticity field around the channel bend. (a and b) Maximum flood tide; (c and d) maximum ebb tide. (a and c) A sharp channel bend with $R/w = 0.82$ in model SIN1; (b and d) a smooth channel bend with $R/w = 1.35$ in model SIN4. R is the minimum radius of curvature along the channel, and w is the channel width. $w = 200$ m for both the sharp and smooth bends. The colormap represents the vorticity, and arrows show the velocity field. Gray lines mark the river banks. The average drag coefficient in each case is also shown.

depth. Consequently, changing the channel width alone can change the fraction of the channel affected by flow separation, and therefore affect C_D. The dependence on w is not shown above as the four models in Figure 8 have the same channel width, but cases with different channel widths will be examined in the following sections.

4.2. Parameter Dependence on Channel Curvature

Previous research identified the dependence of flow separation and energy loss on bend sharpness, which is expressed as R/w with R being the bend radius of curvature and w being the channel width (e.g., Leeder & Bridges, 1975; Leopold, 1960). Although the mathematical model employed in Leopold (1960) was based on a hydraulic jump theory, which is different from our results (see section 5), their exploration of parameter space provides a useful framework. Other researchers have used the sinuosity (e.g., Arcement & Schneider, 1989), which is the ratio of the thalweg length to the straight line length in meanders. However, James (1994) proposed that bend losses are not caused by sinuosity per se, but rather by the curvature of bend. In this research, we also chose bend sharpness as the geometric parameter to describe the effect of meanders on the flow.

Bagnold (1960) argued that the overall resistance in a sinuous channel should increase with decreasing curvature ratio R/w. An adjusted Manning's n that decreases with the curvature ratio was brought forward by James et al. (2001) from a flume experiment, consistent with the idea that the drag increases as bends become sharper. Blanckaert (2015) proposed several dominant geometry parameters controlling flow separation including R/w, where R is the minimum radius of curvature along the channel, and decreased R/w leads to stronger flow separation and thus a larger drag. Natural meanders usually show a variation in radius of curvature with a minimum at the bend apexes (e.g., Parsons, 2003), so in this research, we used the minimum centerline radius of curvature to define R/w and quantify bend sharpness.

The vorticity fields in two channel bends were compared to examine the effects of curvature on flow separation (Figure 9). The two bends have identical channel widths but different minimum radius of curvature and thus different R/w. In the sharp bend (model SIN1), flow separation is strong, and high vorticity is shed from the inner bank and injected into the main flow (Figures 9a and 9c). However, in the smooth bend (model SIN4), flow separation is weak with no change in the main flow width and no recirculating lee eddy is formed. Also, the deflection of the velocity field is minimal, and the high vorticity fluid generated near the wall remains attached (Figures 9b and 9d). Not surprisingly, the form drag in this smooth bend corresponds to a drag coefficient of 0.001–0.003 and the total C_D is much less than that of the sharp bend, that is, an average value of 0.006 compared to 0.01.
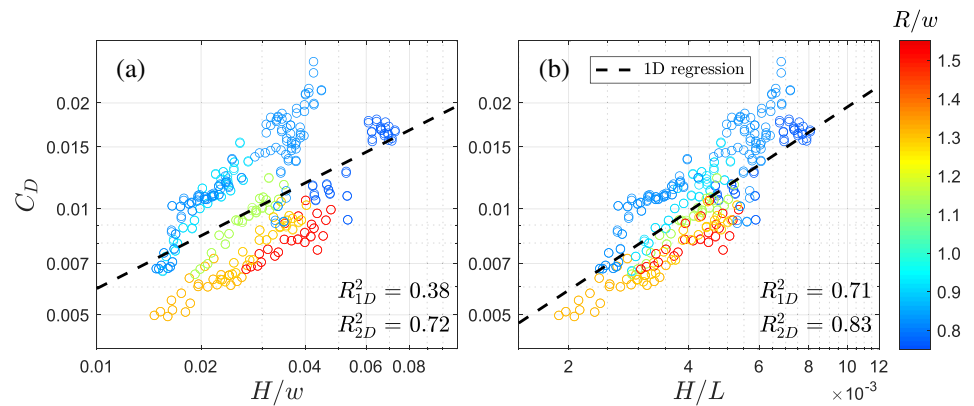
Figure 10. (a) The drag coefficient as a function of H/w with different R/w values. (b) The drag coefficient as a function of H/L with different R/w values. Different colors of the data points denote different R/w values, as is shown on the colorbar. R^2_{1D} represents the statistical R^2 from linear regression of C_D on H/w or H/L; R^2_{2D} represents the statistical R^2 from linear regression of C_D on both H/w or H/L and R/w. The dashed black lines represent the 1-D linear regression on H/w or H/L; the 2-D linear regression is not shown here.

Vorticity in the sharp bend is stronger during flood tide than ebb tide, which is consistent with the stronger flow separation (and larger drag) during the deeper flood tide. The more complex vorticity field during flood tide is probably because deeper water makes flow separation less inhibited by bottom friction, and stronger lateral circulation may also contribute to flow complexity (e.g., Kranenburg et al., 2019). In the smooth bend where flow separation is relatively weak, vorticity is stronger during ebb tide. This is because the current is stronger during ebb tide due to a shallower water depth, creating greater shear and vorticity.

The dependence of flow separation and drag on bend sharpness is not only through the radius of curvature R, but also the width w. Larger w leads to larger lateral variation in depth-averaged velocity and stronger adverse pressure gradient near the inner bank that facilitates flow separation. James et al. (2001) showed that in the cases of wide channels in the laboratory, flow separation occurred and induced considerable energy dissipation, but no such separation occurred in narrow sinuous channels with same radius of curvature. They also observed a significant difference in resistance between the narrow and wide channels due to this additional energy loss associated with flow separation. Our numerical models showed similar results in which flow separation became weaker as channel width decreased while radius of curvature was kept constant. Detailed comparison of flow structure is not shown here, but the calculated C_D from the model results are summarized below in Figure 10.

4.3. Drag Coefficient Diagram

Drag coefficients of all the sinuous models in Table 1 are calculated to examine the influence of H/w and R/w and the results are summarized in Figure 10a. Generally C_D shows an increasing trend with H/w. Within this dependence on H/w, smaller values of R/w are associated with increased C_D. The diagram illustrates how across a range of model configurations, larger H/w and smaller R/w lead to larger C_D, as shown in sections 4.1 and 4.2. The statistical R^2 from the 2-D linear regression of C_D on H/w and R/w indicates that over 70% of the variance for C_D can be explained by these two geometric parameters.

Analysis of the theoretical flow separation model in section 5 suggests to nondimensionalize H using the along-channel bend length L instead of w. The physical explanation of the dependence of C_D on H/L will be shown in section 5, but for the sake of comparison, the diagram as a function of H/L is also plotted in Figure 10b. The conclusion is similar in that C_D increases with H/L and decreases with R/w, but using H/L gives a better collapse of the C_D data and higher R^2 than using H/w.

5. Theoretical Flow Separation Model

In this section, we introduce a theoretical model based on boundary layer separation and compare it with numerical results to understand the parameter dependence of C_D. Outside the boundary layer, flow accelerates as it approaches an island, headland or channel bend, and decelerates after passing by the tip or apex, forming an adverse pressure gradient behind the tip or apex. The adverse pressure gradient is imposed by

the outer potential flow onto the viscous boundary layer, which therefore decelerates and even reverses flow near the boundary and leads to boundary layer separation (Signell & Geyer, 1991). In a sinuous channel with limited width, the boundary layer is not always distinguishable from the main flow, but the basic physics are the same as the "outer potential flow and viscous boundary layer" model. Therefore, in this theoretical model, we will first assume potential channel flow to quantify the flow field and then include friction and viscosity to investigate the boundary layer separation.

5.1. Potential Flow in an Idealized Sinuous Channel

The planform of classical type meanders shows a variation in radius of curvature from a minimum at the bend apexes to infinity at the crossovers between bends (Parsons, 2003). Therefore, in the theoretical model, an idealized flat-bottom channel is built with the centerline radius of curvature described by

$$R = \frac{R_0}{\sin(\pi s/L)},\tag{8}$$

in which s is the along-channel distance and L is the channel bend length. R_0 is the radius of curvature at the bend apex, which is also the smallest radius along the channel. The channel bend is symmetric around the bend apex. We also assume that the radius of curvature increases linearly across the channel (e.g., Leopold, 1960), so that the radius at the inner bank is $R - w/2$ and the radius at the outer bank is $R + w/2$.

The potential flow solution in the idealized channel is derived in Appendix C. The cross-channel velocity profile shows an inversely proportional functional form of $u = K/r$, in which K is a constant and r is the cross-channel distance (Leopold, 1960). Therefore, the maximum velocity appears near the inner bank, which is consistent with the numerical result in Figures 4b1 and 4c as well as other research including Blanckaert (2015) and Kranenburg et al. (2019). The velocity along the inner bank of the channel can be expressed as

$$u_{inner} = \frac{U_0}{\left(\frac{R}{w} - \frac{1}{2}\right)\ln\left(\frac{R+w/2}{R-w/2}\right)},\tag{9}$$

with U_0 being the uniform incident flow and $R = R(R_0, s)$. Flow near the inner bank accelerates as it enters the bend and then decelerates after passing by the bend apex. The maximum inner bank velocity is found at the bend apex.

5.2. Adverse Pressure Gradient Around the Channel Bend

The dominant along-channel momentum balance in the horizontal boundary layer (Signell & Geyer, 1991) is

$$g\frac{\partial \eta}{\partial s} = -u\frac{\partial u}{\partial s} - C_f \frac{u^2}{H}.\tag{10}$$

where u represent the local along-channel velocity instead of the cross-sectional average U, and noninertial effects of curvilinear coordinates are negligible. The unsteady term is negligible because the tidal period is much longer than the timescale of flow passing through one channel bend. The advection term containing v is also relatively small and therefore neglected, and baroclinic effects are ignored because we have assumed homogeneous flow in the theoretical model. Bottom friction is more important than the horizontal viscosity in shallow flows (e.g., Pattiaratchi et al., 1987; Signell & Geyer, 1991; Wolanski et al., 1984), so the horizontal viscous term is also neglected.

In the simplified momentum budget (10), the pressure gradient (the left side term) is balanced by advection (the first term on the right side) and friction (the second term on the right). C_f is the friction coefficient which describes the drag related to bed skin friction, which is the dominant source of drag in the absence of flow separation. C_f is set to be 0.004, a value similar to the C_D of the straight channel numerical model and that predicted by (7) with a bottom roughness of 2 mm and water depth of ~3–4 m.

The pressure gradient associated with potential flow can be obtained by substituting the potential flow solution (9) into (10). We use the inner bank velocity because flow separation happens in the boundary layer near the inner bank. These two right-side terms that determine the pressure gradient are plotted in Figure 11. The friction term always results in a favoring pressure gradient. The advection term causes a favoring pressure gradient before the bend apex where flow is accelerated and sets up an adverse pressure gradient behind
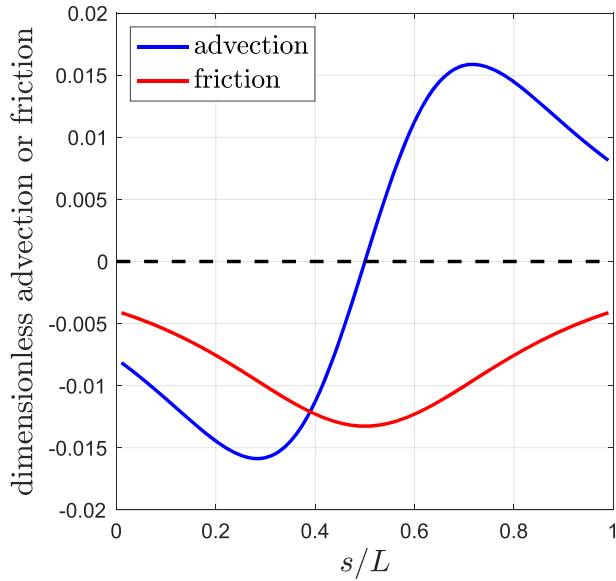
Figure 11. Advection and friction terms in (10) as a function of along-channel distance s in the theoretical flow separation model. L is the along-channel bend length. $s/L = 0.5$ represents the bend apex. Both terms are nondimensionalized by U_0^2/H. As representative values, we set $H/L = 0.005$ and $R/w = 1$.

the bend apex where flow is decelerated. Therefore, flow separation can happen when the advection term exceeds friction and a strong adverse pressure gradient occurs behind the bend apex.

5.3. Parameter Dependence of Flow Separation and Drag Coefficient

Flow separation can be predicted by taking the ratio of the advection term to the friction term. Using the potential flow solution, the advection-friction ratio K_r can be expressed as

$$K_r = -u\frac{\partial u}{\partial s} \Big/ C_f \frac{u^2}{H} = \alpha_1 \alpha_2 \frac{H}{C_f L}, \tag{11a}$$

$$\alpha_1 = \frac{1}{R - w/2}\left(1 - \frac{1}{\left(\frac{R}{w} + \frac{1}{2}\right)\ln\left(\frac{R+w/2}{R-w/2}\right)}\right), \tag{11b}$$

$$\alpha_2 = -\pi R \cot\left(\frac{\pi s}{L}\right). \tag{11c}$$

α_1 is related to potential flow with curvature, that is, $\partial u/\partial R$; α_2 is associated with the sinuous channel shape, that is, $\partial R/\partial s$. For this analysis, s/L is chosen as 0.75 where advection (or adverse pressure gradient) reaches its maximum (Figure 11). Since both α_1 and α_2 are only functions of R_0/w, the advection-friction ratio can be rewritten as

$$K_r = \frac{H}{C_f L}\mathcal{F}\left(\frac{R}{w}\right). \tag{12}$$

Henceforth we drop the subscript of R_0 for convenience and R will represent the smallest centerline radius of curvature along the channel bend. The ratio K_r depends on two dimensionless number, $H/(C_f L)$ and R/w. This dependence on dimensionless water depth and curvature ratio is in agreement with the parameter dependence of C_D in the numerical results in section 4. The water depth H can be either scaled by channel width w or along-channel length L, and both make sense physically. The dependence on H/w lies in the fact that the width of separation zone scales with water depth so the fraction of the main flow impacted by flow separation depends on H/w. H/L emerges by taking the ratio of advection to friction that predicts when flow separation happens. C_f is the bottom friction coefficient, which is a constant in the theoretical model and only varies within a small range in the numerical models, so the effect of C_f is not addressed in detail. $H/(C_f L)$ is analogous to a Reynold's number based on friction instead of viscosity (Pingree & Maddock, 1980; Signell & Geyer, 1991). $H/(C_f L)$ is also called a stability parameter in shallow flows where it is used to categorize island wakes, another example of flow separation (e.g., Jirka & Uijttewaal, 2004). Blanckaert (2010, 2011) reported two similar control parameters of sinuous dynamics $C_f^{-1}H/w$ and w/R, although that analysis was based on a different conceptual model.

The theoretical ratio K_r is plotted as a function of H/L and R/w in Figure 12a. K_r increases with H/L and decreases with R/w, suggesting that flow separation is stronger when H/L is larger and R/w is smaller. This is consistent with the similar dependence of C_D on H/L and R/w in section 4, because C_D increases with greater form drag due to flow separation in the sharp bend models.

$K_r = 1$ is marked by a black line in Figure 12a. For $K_r > 1$, advection dominates friction and flow separation is relatively strong, while for $K_r < 1$, friction dominates advection and flow separation is weak. This theoretical prediction is consistent with our numerical model results. For example, the simulation shown in Figure 9b and 9d, with an $H/L \sim 0.002$–0.003 and $R/w = 1.35$, yields $K_r < 1$ in the theoretical model and exhibits weak flow separation in the simulation. Most of the other simulations fall in the regime of $K_r > 1$ and have relatively strong flow separation and larger C_D.

Leeder and Bridges (1975) proposed a dimensionless graph to predict flow separation as a function of bend sharpness R/w and Froude number F_r. Our research focuses on relatively low F_r flow between 0.1 and 0.2,
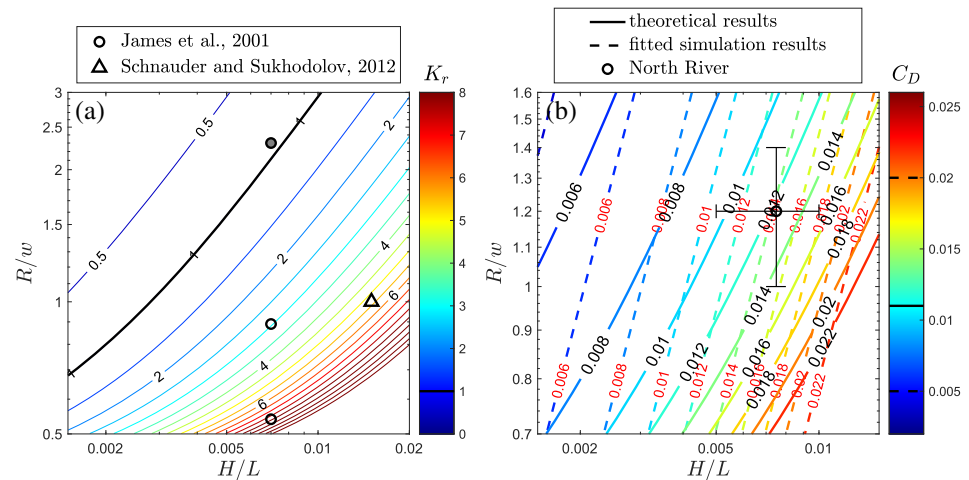
Figure 12. (a) Contours of the ratio of advection to friction K_r as a function of H/L and R/w. $K_r = 1$ is marked by the black lines on the colorbar and contours. Circles represent laboratory experiments by James et al. (2001). The hollow circles show cases where flow separation happens; the circle filled with gray color shows the case where flow separation does not happen. The triangle represents observations by Schnauder and Sukhodolov (2012) at one bend on the Tollense River where flow separation happens. (b) Contours of the drag coefficient C_D. Solid lines represent the C_D predicted by (13) using K_r of the theoretical model. Dashed lines represent the 2-D linear fit of numerical results showed in Figure 10b. The circle shows the estimation of geometric parameters for the North River, with error bars representing spatial and temporal variability. The solid black line on the colorbar represents the average C_D on the North River, and two dashed black lines represent the range of observed C_D on the North River.

and we observed flow separation for an R/w of around 0.7–1.3, which is consistent with that study. James et al. (2001) found that the curvature ratio was 2.3 for a narrow sinuous channel without flow separation and 0.89 and 0.54 for two wide sinuous channels with flow separation, with H/L of approximately 0.007, although this parameter is not directly reported. Their narrow sinuous channel falls above the $K_r = 1$ line on our diagram (Figure 12a) and the wide sinuous channels are below the line, consistent with the theoretical model. A counter example comes from the laboratory channel in Kashyap et al. (2012) which had $H/L = 0.042$ and $R/w = 1.5$ and yet flow separation did not occur. The theoretical model is based on the shallow flow assumption, that is, bottom friction dominates viscosity, and as a result the theoretical prediction may be less applicable in laboratory flumes where viscosity and friction from sidewalls may have greater influence on the total drag. We can also apply the theoretical model to field observations from the literature. Flow separations observed at two sharp bends on the River Dean, with $H/L \approx 0.04$, $R/w = 0.9$ and 1.4, respectively (Ferguson et al., 2003), and on the Tollense River at a bend with $H/L = 0.015$ and $R/w = 1.0$ (Schnauder & Sukhodolov, 2012) were consistent with the prediction given by Figure 12a. These two rivers were both relatively deeper than our models. In many rivers, the existence of a point bar decreases water depth near the inner bend and may inhibit flow separation such that rivers must be deeper than tidal channels with similar bend sharpness for flow separation to happen.

While the influences of H/L and R/w are investigated in this research, the bottom friction coefficient C_f also appears in the theoretical result (12). The bottom roughness is uniform in all the numerical models, so there is not sufficient parameter range to investigate the influence of C_f on flow separation. C_f depends on water depth, but the influence of water depth is greater on H/L than C_f. James et al. (2001) reported that vegetation can inhibit flow separation in channel bends and decrease the overall drag. Their research supports our theoretical result that increasing C_f will decrease the advection-friction ratio K_r and suppress flow separation, although in James et al. (2001) C_f is increased by vegetation stem friction rather than bottom roughness.

Comparing Figure 10b to Figure 12a, we can observe similar dependencies of K_r and C_D on H/L and R/w. K_r is the advection-friction ratio that predicts flow separation in the theoretical model, while C_D is dominated by form drag in sharp sinuous channels according to the numerical results. This correspondence between the theoretical model and numerical simulations provides further support that the increased drag coefficient is due to flow separation, and leads to the possibility of predicting C_D using the theoretical flow separation

model. The ratio K_r can serve as a correction coefficient or amplification factor to the drag coefficient, that is, $C_D = \mathcal{G}(K_r)C_f$. We choose a simple linear expression,

$$C_D = (K_r + 1)C_f. \tag{13}$$

Although secondary circulation can be another contributing factor in increasing drag, this is not included in (13) as the effect of flow separation is dominant in the sharp channel bends of our models. This linear expression does not account for the effect of C_f on flow separation drag either, because it cancels with the C_f in the denominator of K_r. These results assume a fixed value for C_f, but this linear expression, as a speculation, can be used to represent the effects of the two geometric parameters H/L and R/w on C_D.

The predicted C_D given by (13) is plotted as the dashed line in Figure 8, which agrees reasonably well with our numerical results. The parameter H/L is converted to H/w for the convenience of comparison. In Figure 12b, the 2-D linear fit of the numerical results (Figure 10b) is compared with the theoretical prediction by (13). The theoretical prediction shows consistency with the numerical results in the increasing trend with H/L and decreasing trend with R/w as well as the magnitude of C_D, even though we are only using a linear relationship (13) with constant C_f. For the North River estuary that initially motivated this study, the two geometric parameters are estimated from Kranenburg et al. (2019), with average $H/L \approx 0.008$ and $R/w \approx 1.2$. Using these values, the effective drag in the North River predicted by Figure 12b is around 0.012 ± 0.003, where as observations found an average C_D of ~0.011, ranging between 0.005 and 0.02 (Kranenburg et al., 2017). It is also worthwhile to note that the parameter dependence discussed above is only correct in the regime where flow separation happens. When there is no flow separation, for example, when water is very shallow or the bend is very smooth, C_D will either decrease with H as is predicted by (7) for straight channels, or show a different parameter dependence if the increased drag is predominately due to secondary circulation.

6. Discussion

6.1. Flow Separation and Drag Increase in Sinuous Channels

This research shows that the drag coefficient can be increased by channel meanders as a result of flow separation. Therefore, we suggest modifications to traditional drag coefficients for flow in sinuous tidal channels, for example, an increase of up to a factor of 2–7 depending on the strength of flow separation. Such a substantial increase to the drag can increase water level slope and result in considerable water level changes along the channel, which influences wetland inundation and regulates the distribution of vegetation. The increased drag in sinuous channels can also affect tidal propagation (larger amplitude decay and increased phase lag) and potentially storm surge flooding. A sinuous planform may also enhance nonlinear tidal transformation and affect the growth of overtides, which then affects sediment transport.

Apart from the effects of increased drag, flow separation due to channel curvature has the potential to enhance erosion near the inner bank at bend apex, because it increases local velocity and injects fluid from the inner bank to the main flow. Erosion associated with flow separation could alter the sinuous channel morphology, for example, by the erosion of a point bar. Reversal in the lateral circulation associated with the baroclinic pressure gradient has also been suggested as enhancing erosion near the inner bank and inhibiting formation of a point bar (Kranenburg et al., 2019). Flow separation together with the reversed lateral circulation can explain the absence of a point bar in many sharp bends in tidal meanders, while the absence of a point bar in turn allows for flow separation and the reversed lateral circulation. Flow separation increases deposition in the recirculating dead zone beyond the bend apex where currents are very weak, for example, Schmidt (1990) found that sandbars form beneath recirculation zones in the Colorado River in the Grand Canyon. As a result, sandbars can grow in the lee of bends where flow separation occurs, and this growth may act differently in unidirectional flow of rivers than the bidirectional flow of tidal channels. The dead zone created by flow separation could also affect along-channel scalar transport by trapping tracers and increasing longitudinal mixing and dispersion (Thackston & Schnelle, 1970).

Key parameters that influence the increased drag coefficient were discussed in this paper—H/L (or H/w) and R/w—but other factors may also affect flow separation drag. Signell and Geyer (1991) mentioned that local acceleration can cause an adverse pressure gradient over headland scales comparable to the tidal excursion (5–10 km), which therefore impacts the strength of flow separation and magnitude of drag. In the sinuous

channels of this study, the channel bends are around 100–1,000 m in length, which is much smaller than the tidal excursion so the effect of tidal flow unsteadiness can be neglected. However, channel bends with lengths of up to 10 km are also observed in nature (e.g., Marani et al., 2002) and the unsteadiness associated with tidal currents need to be considered in these cases. In addition, while the velocity field is conventionally considered to be reset at the cross-over point between channel bends (e.g., Abad & Garcia, 2009), interactions between meanders may occur for closely spaced bends (e.g., Leopold, 1960). The vortices shed from an upstream bend due to flow separation can interact with the vorticity field of the downstream bends (Figure 9), and the enhanced instability through multiple bends may affect flow separation and the drag.

This research focused on the increased drag coefficient in sinuous channels associated with flow separation. Secondary circulation created by the sinuous planform can also increase drag by enhancing the lateral velocity and bottom stress (e.g., Chang, 1984; Pein et al., 2018). The drag coefficient increase due to secondary circulation is generally less than 30% in our model results, which is modest compared to the total drag increase associated with flow separation in these very sharp channel bends (a factor of 2–7). However, in the channel bends that are less sharp, secondary circulation could be a bigger factor in increasing drag. Blanckaert and De Vriend (2010) and Blanckaert (2011) quantitatively expressed the magnitude of secondary circulation as a function of $C_f^{-1}H/w$ and w/R, and this provides a framework for exploring the parameter dependence of the C_D associated with secondary circulation. In addition to the direct effects of secondary circulation discussed above, interactions between the secondary circulation and flow separation (e.g., Figure 5) or stratification could also affect the total drag, and are topics which require further research.

In the numerical study, C_D is calculated based on U, the channel average velocity, as the velocity field shows large lateral variations in sinuous models. However, in field observations the channel average velocity is hard to directly measure, and C_D is usually applied to velocity measurements at one location. If field observations are made in the center of the channel where the main flow is accelerated as a result of flow separation, U in the denominator of (3) will be overestimated and the measured C_D will become smaller than that predicted by this study. On the contrary, if the current meter is located close to the dead zone, the measured C_D will become larger instead.

6.2. Similarity and Differences Between Rivers and Tidal Channels

River meanders and tidal meanders show strong similarity in their planform geometry (Marani et al., 2002). The similarity lies in the bend sharpness, which is customarily quantified as R/w. Two thirds of the R/w values lie between 1.5 and 4.3 in a sample of 50 rivers (Leopold & Wolman, 1960), and R/w is found to be 1.6–5 in tidal meanders (Marani et al., 2002). Very sharp bends in river meanders can have an R/w as small as 1.0 (Schnauder & Sukhodolov, 2012) and 0.6 (Nanson, 2010), and in tidal meanders the smallest R/w can reach 0.5 near sharp bend apexes (Marani et al., 2002). Previous studies have also found that fluvial and tidal meanders have similar channel sinuosity (the ratio between along-channel distance to meander wavelength) and similar ratios of meander wavelength to channel width, for widths and wavelengths spanning 3 to 4 orders of magnitude (Leopold & Wolman, 1960; Leopold et al., 1995; Marani et al., 2002).

Key morphological differences between river meanders and tidal meanders lie in their aspect ratio (channel width to depth, w/H), and typically, the cross-channel depth distribution. In river channel bends, the aspect ratio usually falls between 10 and 50 (Millar, 2000). Tidal flat channels tend to have aspect ratios similar to rivers, in the range of 8–50 (Marani et al., 2002), but in salt marsh channels the aspect ratio is typically around 6 (Marani et al., 2002), making them narrower or deeper than river meanders. Vegetation along salt marsh channels can help stabilize banks, reducing channel migration and further steepening banks (Gabet, 1998; Redfield, 1972). The cross-channel depth profile of tidal channels may also differ from rivers, where point bars are commonly found at the inside of bends (Leopold & Wolman, 1960) due to the cross-channel circulation and sediment transport that leads to shallower bathymetry at the inside of bends and deeper at the outside. While point bars also can occur in tidal channels (Barwis, 1977; Fagherazzi et al., 2004), in some sharp tidal channel bends the cross-channel bathymetry is relatively uniform, with an absence of a distinct point bar (e.g., Barwis, 1977; Kranenburg et al., 2019; Nidzieko et al., 2009).

The study site of the North River does not have distinct point bars, and the numerical models have symmetric lateral depth structure. A point bar can enhance the friction near the inner bank, that is, increase the C_f and decrease the effective depth H in (12), and thus inhibit flow separation and decrease the form drag. On the other hand, the presence of a point bar can decrease the effective width and increase the effective R/w, which reduces the bend sharpness and the strength of flow separation. Marriott (1998) found in the

laboratory that when the flow went overbank and became very shallow near the inner bend, flow reversal and separation were no longer observed, which is similar to the influence of point bars. The prevalence of point bars may explain why flow separation and the associated drag increase are less common in the river literature. Therefore, the effect of cross-channel bathymetry profile needs to be carefully examined in the prediction of flow separation and drag coefficient. On the other hand, flow separation is reported in some rivers that are relatively deeper than our models (e.g., Ferguson et al., 2003; Schnauder & Sukhodolov, 2012), so this form drag may still be expected to occur in relatively deep rivers or tidal channels with a point bar.

Rivers and tidal channels also differ markedly in their hydrodynamic forcing. Rivers have unidirectional fluvial discharge, while tidal channels are influenced by bidirectional tidal flow. Estuarine tidal channels also have inputs of freshwater that create density differences and influence the dynamics. Baroclinic pressure gradients and stratification contribute to the flow structure in many tidal channels, including by modifying turbulence (Geyer, 1993) and lateral circulation (Chant & Wilson, 1997; Nidzieko et al., 2009). The differences in forcing correspond with differences in time scales of variability between rivers and tidal channels. Bidirectional tidal flow changes regularly at semidiurnal to spring-neap periods, while in rivers, major discharge events may occur once a year or less frequently.

The theoretical model is based on the assumption that fluid is homogeneous. In our numerical models, the estuary was weakly stratified during early flood tide and early ebb tide and was vertically well-mixed during other tidal stages. Differences in lateral circulation were also observed between flood and ebb tides, associated with lateral baroclinic pressure gradients. Although the effects of stratification and lateral circulation on C_D require further investigation, the theoretical model without these factors can account for most of the variability in C_D, suggesting that stratification and baroclinic pressure gradients are secondary factors in weakly stratified channels. Conclusions of this study are not only restricted to estuarine tidal channels with mixed fresh and salt water but can also be applied to tidal freshwater or fluvial rivers with similar planform and cross-sectional geometry.

7. Conclusion

Increased drag coefficients are found in sinuous channel models, consistent with observations from the North River estuary. This drag increase leads to faster tidal amplitude decay and larger tidal phase lag in tidal channels with curvature. The increased drag coefficient is mainly due to flow separation, which creates a low pressure zone in the lee of bends and produces form drag. The curved estuarine channel also has larger energy dissipation as a result of decreased effective channel width, increased velocity in the center of the channel, and weakened stratification. The increased drag coefficient in sinuous channels depends on two geometric parameters, that is, it increases with H/L, where H is the water depth and L is the along-channel bend length, and decreases with R/w, where R is the bend radius of curvature and w is channel width. A theoretical boundary layer separation model successfully represents this parameter dependence, which is based on the relative dominance of advection and friction. The theoretical model suggests that flow separation shows similar dependence on H/L and R/w and predicts conditions for flow separation to happen: $R/w < 1$ for "shallow" channels, for example, $H/L \sim 0.003$–0.005 or an aspect ratio of $\sim$20–40; and $R/w < 1.5$ for "deep" channels, for example, $H/L \sim 0.005$–0.01 or an aspect ratio of $\sim$10–20. As a result, the drag coefficient can increase by a factor of 2–7 depending on channel geometry and strength of flow separation. A point bar can decrease water depth near the inner bank and potentially inhibit flow separation and prevent the drag increase. Although we focused on estuarine channels without a point bar, this research still suggests that the increased drag coefficient associated with flow separation is expected in river or tidal meanders with a point bar, when the bend is sharp and channel is deep enough.

Appendix A: Sinuous Channel Shape

The mathematical expressions for setting sinuous channel shapes are proposed by Langbein and Leopold (1970) based on the theory of minimum variance. The direction angles of channel centerline are set as

$$\theta = A \sin(s), \tag{A1}$$

in which A determines the maximum angle of deviation from the mean downstream direction. The Cartesian expression of channel centerline is generated in an integral form with respect to the angle and along-channel distance,
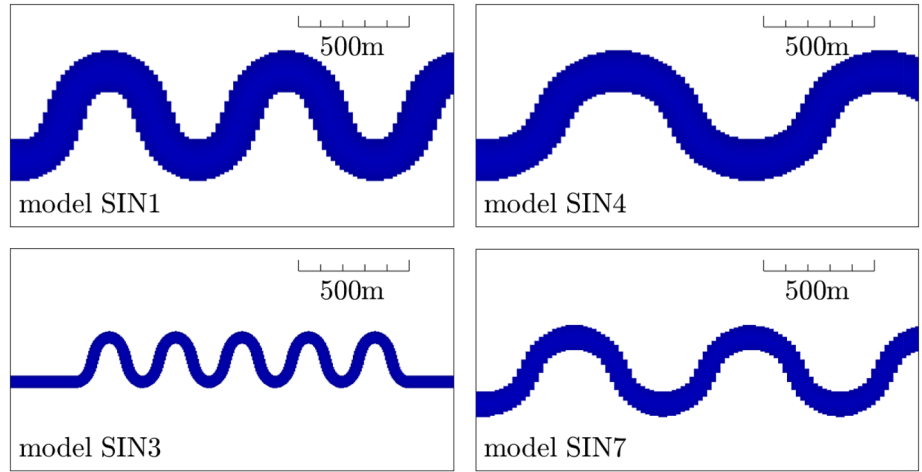
Figure A1. Some channel shapes used in the models. The scale is as marked in the plot.

$$x = X \int \cos\theta \, ds; \quad y = Y \int \sin\theta \, ds. \tag{A2}$$

X, Y determine the Cartesian length (L_x) and Cartesian width (L_y) of the channel bend, respectively. Four representative channel shapes are exhibited in Figure A1.

Appendix B: Integral Form of the Momentum Budget

Simplify (4) and the integral form of the momentum equation for the straight channel can be written as

$$\int_{A_{CS1}} p \, dA - \int_{A_{CS2}} p \, dA + \int_{A_b} p\xi_x \, dA + \int_{A_b} \tau_{bx} \, dA = 0. \tag{B1}$$

where A_{CS1} and A_{CS2} represent the cross-sectional areas at each end of the control volume and A_b represents the area of the channel bed. ξ_x corresponds to the projection in x direction. There is no integrated pressure on the sidewalls because the projected area in the x direction is 0 in the straight model so the integral over A_w has been removed from (4). The unsteady and advection terms are neglected, and only barotropic pressure is included because baroclinic effects are small.

Momentum balance is achieved among the total pressure difference force (Figure B1)

$$P_{diff,total} = \int_{A_{CS1}} p \, dA - \int_{A_{CS2}} p \, dA, \tag{B2}$$

the pressure force exerted by the decreasing thalweg depth along the channel (the bottom-slope effect)

$$P_{slope} = \int_{A_b} p\xi_x \, dA = \int_{A_b} \rho g(h + \eta)\xi_x \, dA, \tag{B3}$$
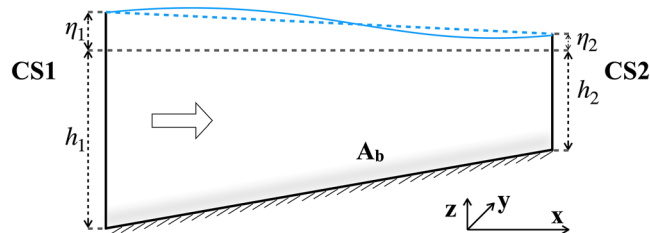

Figure B1. Schematic of the side view of the straight channel with decreasing thalweg depth. $CS1$ and $CS2$ represent the cross sections at each end of the control volume, and A_b represents the channel bed. h_1 and h_2 represent the depth of channel bed below mean water level; η_1 and η_2 represent the water level. h_1, h_2, η_1, and η_2 are functions of y. The solid blue line is the water level, and the dashed blue line is the linear approximation of the water level.
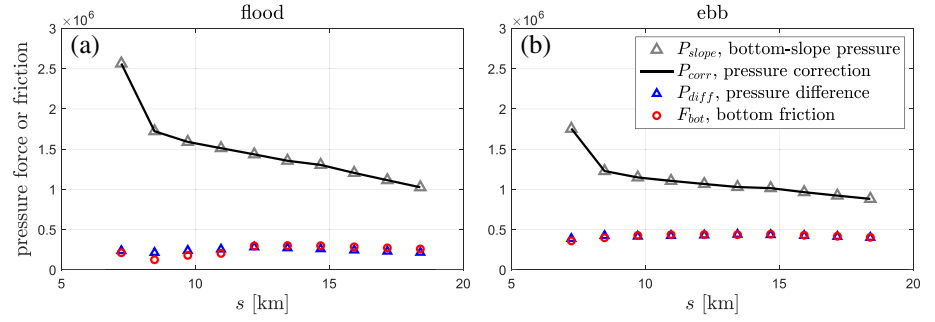
Figure B2. Pressure force and bottom friction in the momentum budget (B1) of the straight channel. (a) Maximum flood tide. (b) Maximum ebb tide. Blue triangles represent the corrected pressure difference in (B5), and red circles represent the bottom friction. Gray triangles are the pressure force associated with along-channel depth decrease calculated directly by integrating over the bottom using (B3). Black lines are the pressure correction term used to cancel the bottom slope effect calculated by using (B4).

and the bottom friction F_{bot} (the last term in (B1)). A considerable part of $P_{diff,total}$ is contributed by the channel depth difference between $CS1$ and $CS2$ and this part is exactly canceled by the bottom-slope pressure force P_{slope} in the momentum budget. To quantify the pressure difference created only by the water level and get rid of the bottom-slope effect, we write a pressure correction term by applying linear approximation (Figure B1) to the water level field in (B3) (i.e., the water level linearly changes along the channel)

$$P_{corr} = \int_0^w \frac{1}{2}(h_1 + \eta_1 + h_2 + \eta_2)(h_1 - h_2)\mathrm{d}y. \tag{B4}$$

The bottom-slope pressure force P_{slope} in (B3) is calculated directly by integrating over the bottom A_w. The pressure correction term P_{corr} in (B4) is calculated based on the linear approximation by using only water level and channel depth at the ends of the control volume. P_{corr} can balance P_{slope} (Figure B2) and the remaining "form drag" in the straight channel is 0, by subtraction B4 from B3. Therefore, we can write the corrected pressure difference force by subtracting P_{corr} from (B2)

$$P_{diff} = \int_{A_{CS1}} p\mathrm{d}A - \int_{A_{CS2}} p\mathrm{d}A - P_{corr}, \tag{B5}$$

which only accounts for the pressure difference associated with water level and does not incorporate the bottom-slope effect. In the straight channel, the corrected pressure difference P_{diff} is generally equal to the bottom friction F_{bot} for both flood and ebb tide (Figure B2), indicating that the momentum budget closes with these two terms, and corresponds to a drag coefficient of 0.003–0.004, consistent with the calculation in section 3.1. Therefore, the pressure correction based on the linear approximation is effective for removing the bottom-slope effect in the straight channel, and this same approach can be applied to the sinuous channel. The pressure force associated with bottom slope is much larger than the pressure difference created by water level and the bottom friction (Figure B2), as the bottom slope is greater than the water level slope, which again illustrates the need to remove the bottom-slope effect in calculating the momentum budget.

The pressure difference in the sinuous channel is calculated in a similar way as (B5) to remove the pressure force associated with along-channel depth decrease. The form drag of the sinuous channel is also calculated by subtracting the pressure correction term P_{corr} from the third right-side term in (4),

$$P_{form} = \int_{A_w + A_b} p\xi_x\mathrm{d}A - P_{corr}, \tag{B6}$$

to remove the bottom-slope effect and only keep the form drag associated with water level variations around the bend. A_w is included in (B6) for the sinuous channel, which did not appear in the straight channel where there is no wall normal to the x direction.

Appendix C: Potential Flow Model

Assume potential flow in a flat-bottom channel and the radius of curvature of the centerline is

$$R = \frac{R_0}{\sin(\pi s / L)}, \tag{C1}$$

in which s is the along-channel distance and L is the channel bend length. R_0 is the radius of curvature at the bend apex, which is also the smallest radius along the channel. The channel bend is symmetric around the bend apex. We also assumed that the radius of curvature increases linearly across the channel (e.g., Leopold, 1960), so that the radius at the inner bank is $R - w/2$ and the radius at the outer bank is $R + w/2$, where w is the channel width.

Assume the flow entering the bend is uniform with velocity U_0 and water depth H. The along-channel Bernoulli equation is

$$gH(s, r) + \frac{1}{2}u(s, r)^2 = gH_0 + \frac{1}{2}U_0^2, \tag{C2}$$

where both water depth H and velocity u are a function of along-channel distance s and cross-channel distance r. We assume no lateral or vertical velocity so u only represents streamwise velocity. Differentiating (C2) in the cross-channel direction gives

$$g\frac{\partial H}{\partial r} = g\frac{\partial(H_0 + \eta)}{\partial r} = g\frac{\partial \eta}{\partial r} = -u\frac{\partial u}{\partial r}, \tag{C3}$$

with η being surface elevation. The cross-channel Euler equation is

$$g\frac{\partial \eta}{\partial r} = \frac{u^2}{r}. \tag{C4}$$

Substituting (C3) into (C4) and we obtain

$$u = \frac{K}{r}. \tag{C5}$$

The cross-channel velocity profile is inversely proportional to cross-channel distance with K being a constant at each cross section (Leopold, 1960).

Combining the along river conservation of mass

$$\int_{R-w/2}^{R+w/2} u(s, r)H(s, r)\mathrm{d}r = U_0 H_0 w \tag{C6}$$

and the along-channel Bernoulli Equation C2, we get an expression to solve for K (Shapiro & Sonin, 2018),

$$U_0 H_0 w = KH_0 \left(1 + \frac{U_0^2}{2gH_0}\right) \ln\frac{R + w/2}{R - w/2} - \frac{K^3}{4g(R - w/2)^2}\left(1 - \left(\frac{R - w/2}{R + w/2}\right)^2\right). \tag{C7}$$

The water level differences are negligible compared to the total water depth in the mass flux (but the water level change related to Bernoulli should never be neglected), so K can be approximated as

$$K \approx \frac{U_0 w}{\ln\left(\frac{R+w/2}{R-w/2}\right)}. \tag{C8}$$

Therefore, we get the inner bank velocity at $r = R - w/2$,

$$u_{inner} = \frac{U_0}{\left(\frac{R}{w} - \frac{1}{2}\right)\ln\left(\frac{R+w/2}{R-w/2}\right)}, \tag{C9}$$

with $R = R(R_0, s)$.

Data Availability Statement

Model data generated in this study are available online (at https://doi.org/10.5281/zenodo.3711648).

References

Abad, J. D., & Garcia, M. H. (2009). Experiments in a high-amplitude Kinoshita meandering channel: 2. Implications of bend orientation on bed morphodynamics. *Water Resources Research*, *45*, W02402. https://doi.org/10.1029/2008WR007017

Apmann, R. P. (1964). A case history in theory and experiment: Fluid flow in bends. *Isis*, *55*(4), 427–434.

Arcement, G. J., & Schneider, V. R. (1989). Guide for selecting Manning's roughness coefficients for natural channels and flood plains.

Aubrey, D. G., & Speer, P. E. (1985). A study of non-linear tidal propagation in shallow inlet/estuarine systems Part I: Observations. *Estuarine, Coastal and Shelf Science*, *21*(2), 185–205.

Bagnold, R. A. (1960). *Some aspects of the shape of river meanders*. Washington, DC: US Government Printing Office.

Barwis, J. H. (1977). Sedimentology of some South Carolina tidal-creek point bars, and a comparison with their fluvial counterparts. *Fluvial Sedimentology*, *5*, 129–160.

Blanckaert, K. (2010). Topographic steering, flow recirculation, velocity redistribution, and bed topography in sharp meander bends. *Water Resources Research*, *46*, W09506. https://doi.org/10.1029/2009WR008303

Blanckaert, K. (2011). Hydrodynamic processes in sharp meander bends and their morphological implications. *Journal of Geophysical Research*, *116*, F01003. https://doi.org/10.1029/2010JF001806

Blanckaert, K. (2015). Flow separation at convex banks in open channels. *Journal Of Fluid Mechanics*, *779*, 432–467.

Blanckaert, K., & de Vriend, H. J. (2003). Nonlinear modeling of mean flow redistribution in curved open channels. *Water Resources Research*, *39*(12), 167–14.

Blanckaert, K., & De Vriend, H. J. (2004). Secondary flow in sharp open-channel bends. *Journal of Fluid Mechanics*, *498*, 353–380.

Blanckaert, K., & De Vriend, H. J. (2010). Meander dynamics: A nonlinear model without curvature restrictions for flow in open-channel bends. *Journal of Geophysical Research*, *115*, F04011. https://doi.org/10.1029/2009JF001301

Blanckaert, K., Kleinhans, M. G., McLelland, S. J., Uijttewaal, W. S. J., Murphy, B. J., van de Kruijs, A., et al. (2013). Flow separation at the inner (convex) and outer (concave) banks of constant-width and widening open-channel bends. *Earth Surface Processes and Landforms*, *38*(7), 696–716.

Buijsman, M. C., & Ridderinkhof, H. (2008). Variability of secondary currents in a weakly stratified tidal inlet with low curvature. *Continental Shelf Research*, *28*(14), 1711–1723.

Chang, H. H. (1984). Variation of flow resistance through curved channels. *Journal of Hydraulic Engineering*, *110*(12), 1772–1782.

Chant, R. J. (2002). Secondary circulation in a region of flow curvature: Relationship with tidal forcing and river discharge. *Journal of Geophysical Research*, *107*(C9), 14–1.

Chant, R. J., & Wilson, R. E. (1997). Secondary circulation in a highly stratified estuary. *Journal of Geophysical Research*, *102*(C10), 23,207–23,215.

Chow, V. T. (1959). Development of uniform flow and its formulas. In *Open-channel hydraulics* (pp. 89–127). New York City, NY: McGraw-Hill Book Company, Inc.

Constantinescu, G., Kashyap, S., Tokyay, T., Rennie, C. D., & Townsend, R. D. (2013). Hydrodynamic processes and sediment erosion mechanisms in an open channel bend of strong curvature with deformed bathymetry. *Journal of Geophysical Research: Earth Surface*, *118*, 480–496. https://doi.org/10.1002/jgrf.20042

Fagherazzi, S., Gabet, E. J., & Furbish, D. J. (2004). The effect of bidirectional flow on tidal channel planforms. *Earth Surface Processes and Landforms: The Journal of the British Geomorphological Research Group*, *29*(3), 295–309.

Ferguson, R. I., Parsons, D. R., Lane, S. N., & Hardy, R. J. (2003). Flow in meander bends with recirculation at the inner bank. *Water Resources Research*, *39*(11), 299–13.

Frothingham, K. M., & Rhoads, B. L. (2003). Three-dimensional flow structure and channel change in an asymmetrical compound meander loop, Embarras River, Illinois. *Earth Surface Processes and Landforms: The Journal of the British Geomorphological Research Group*, *28*(6), 625–644.

Gabet, E. J. (1998). Lateral migration and bank erosion in a saltmarsh tidal channel in San Francisco Bay, California. *Estuaries*, *21*(4), 745–753.

Geyer, W. R. (1993). The importance of suppression of turbulence by stratification on the estuarine turbidity maximum. *Estuaries*, *16*(1), 113–125.

Gill, A. E. (1982). *Atmosphere-ocean dynamics*. San Diego, CA: Academic Press.

Grant, W. D., & Madsen, O. S. (1982). Movable bed roughness in unsteady oscillatory flow. *Journal of Geophysical Research*, *87*(C1), 469–481.

Haidvogel, D. B., Arango, H., Budgell, W. P., Cornuelle, B. D., Curchitser, E., Di Lorenzo, E., et al. (2008). Ocean forecasting in terrain-following coordinates: Formulation and skill assessment of the regional ocean modeling system. *Journal of Computational Physics*, *227*(7), 3595–3624.

James, C. S. (1994). Evaluation of methods for predicting bend loss in meandering channels. *Journal of Hydraulic Engineering*, *120*(2), 245–253.

James, C. S., Liu, W., & Myers, W. R. C. (2001). Conveyance of meandering channels with marginal vegetation. *Proceedings of the Institution of Civil Engineers-Water and Maritime Engineering*, *148*(2), 97–106.

Jamieson, E. C., Ruta, M. A., Rennie, C. D., & Townsend, R. D. (2013). Monitoring stream barb performance in a semi-alluvial meandering channel: Flow field dynamics and morphology. *Ecohydrology*, *6*(4), 611–626.

Jirka, G. H., & Uijttewaal, W. S. J. (2004). Shallow flows: A definition. *Shallow Flows*, 3–11.

Kadlec, R. H. (1990). Overland flow in wetlands: Vegetation resistance. *Journal of Hydraulic Engineering*, *116*(5), 691–706.

Kalkwijk, J. P. T., & Booij, R. (1986). Adaptation of secondary flow in nearly-horizontal flow. *Journal of Hydraulic Research*, *24*(1), 19–37.

Kashyap, S., Constantinescu, G., Rennie, C. D., Post, G., & Townsend, R. (2012). Influence of channel aspect ratio and curvature on flow, secondary circulation, and bed shear stress in a rectangular channel bend. *Journal of Hydraulic Engineering*, *138*(12), 1045–1059.

Kranenburg, W. M., Geyer, W. R., Garcia, A. M. P., & Ralston, D. K. (2019). Reversed lateral circulation in a sharp estuarine bend with weak stratification. *Journal of Physical Oceanography*, *49*, 1619–1637.

Kranenburg, W. M., Geyer, R., & Ralston, D. K. (2017). Observations of salinity and flow velocity structure in a narrow and curvy tidal river. In *24th Biennial CERF Conference*, CERF.

Kunkel, C. M., Hallberg, R. W., & Oppenheimer, M. (2006). Coral reefs reduce tsunami impact in model simulations. *Geophysical Research Letters*, *33*, L23612. https://doi.org/10.1029/2006GL027892

Langbein, W. B. (1963). The hydraulic geometry of a shallow estuary. *Hydrological Sciences Journal*, *8*(3), 84–94.

Langbein, W. B., & Leopold, L. B. (1966). River meanders—Theory of minimum variance. *USGS Prof., Paper 422-H*, *15*, 1966.

Langbein, W. B., & Leopold, L. B. (1970). *River meanders and the theory of minimum variance* (pp. H1–H15). Washington, DC: US Government Printing Office.

Leeder, M. R., & Bridges, P. H. (1975). Flow separation in meander bends. *Nature*, *253*, 1–2.

Lentz, S. J., Davis, K. A., Churchill, J. H., & DeCarlo, T. M. (2017). Coral reef drag coefficients—Water depth dependence. *Journal of Physical Oceanography*, *47*(5), 1061–1075.

Leopold, L. B. (1960). *Flow resistance in sinuous or irregular channels*. Washington, DC: US Government Printing Office.

Leopold, L. B., Collins, J. N., & Collins, L. M. (1993). Hydrology of some tidal channels in estuarine marshland near San Francisco. *Catena Verlag*, *20*, 469–493.

Leopold, L. B., & Wolman, M. G. (1960). River meanders. *Geological Society of America Bulletin*, *71*(6), 769–793.

Leopold, L. B., Wolman, M. G., & Miller, J. P. (1995). *Fluvial processes in geomorphology*. Mineola, NY: Dover Publications.

Li, C., Valle-Levinson, A., Atkinson, L. P., Wong, K. C., & Lwiza, K. M. M. (2004). Estimation of drag coefficient in James River Estuary using tidal velocity data from a vessel-towed ADCP. *Journal of Geophysical Research*, *109*, C03034. https://doi.org/10.1029/2003JC001991

Marani, M., Lanzoni, S., Zandolin, D., Seminara, G., & Rinaldo, A. (2002). Tidal meanders. *Water Resources Research*, *38*(11), 1225. https://doi.org/10.1029/2001WR000404

Marriott, M. J. (1998). Hydrodynamics of flow around bends in meandering and compound channels. (PhD thesis), University of Herfordshire.

McCabe, R. M., MacCready, P., & Pawlak, G. (2006). Form drag due to flow separation at a headland. *Journal of Physical Oceanography*, *36*(11), 2136–2152.

Millar, R. G. (2000). Influence of bank vegetation on alluvial channel patterns. *Water Resources Research*, *36*(4), 1109–1118.

Monismith, S. G., Hirsh, H., Batista, N., Francis, H., Egan, G., & Dunbar, R. B. (2019). Flow and drag in a seagrass bed. *Journal of Geophysical Research: Oceans*, *124*, 2153–2163. https://doi.org/10.1029/2018JC014862

Nanson, R. A. (2010). Flow fields in tightly curving meander bends of low width-depth ratio. *Earth Surface Processes and Landforms: The Journal of the British Geomorphological Research Group*, *35*(2), 119–135.

Nepf, H. M. (1999). Drag, turbulence, and diffusion in flow through emergent vegetation. *Water resources research*, *35*(2), 479–489.

Nezu, I. (1993). Turbulence in open-channel flows. IAHR-monograph.

Nidzieko, N. J., Hench, J. L., & Monismith, S. G. (2009). Lateral circulation in well-mixed and stratified estuarine flows with curvature. *Journal of Physical Oceanography*, *39*(4), 831–851.

Nikuradse, J. (1933). *Strömungsgesetze in rauhen rohren*. Berlin: VDI-Verlag.

Parsons, D. R. (2003). *Flow separation in meander bends* (PhD thesis). University of Sheffield.

Pattiaratchi, C., James, A., & Collins, M. (1987). Island wakes and headland eddies: A comparison between remotely sensed data and laboratory experiments. *Journal of Geophysical Research*, *92*(C1), 783–794.

Pein, J., Valle-Levinson, A., & Stanev, E. V. (2018). Secondary circulation asymmetry in a meandering, partially stratified estuary. *Journal of Geophysical Research: Oceans*, *123*, 1670–1683. https://doi.org/10.1002/2016JC012623

Pingree, R. D., & Maddock, L. (1980). The effects of bottom friction and Earth's rotation on an island's wake. *Journal of the Marine Biological Association of the United Kingdom*, *60*(2), 499–508.

Redfield, A. C. (1972). Development of a New England salt marsh. *Ecological monographs*, *42*(2), 201–237.

Rogers, J. S., Maticka, S. A., Chirayath, V., Woodson, C. B., Alonso, J. J., & Monismith, S. G. (2018). Connecting flow over complex terrain to hydrodynamic roughness on a coral reef. *Journal of Physical Oceanography*, *48*(7), 1567–1587.

Rozovskii, I. L. (1957). *Flow of water in bends of open channels*. Kiev: Academy of Sciences of the Ukrainian SSR.

Schmidt, J. C. (1990). Recirculating flow and sedimentation in the Colorado River in Grand Canyon, Arizona. *The Journal of Geology*, *98*(5), 709–724.

Schnauder, I., & Sukhodolov, A. N. (2012). Flow in a tightly curving meander bend: Effects of seasonal changes in aquatic macrophyte cover. *Earth Surface Processes and Landforms*, *37*(11), 1142–1157.

Seim, H., Blanton, J., & Elston, S. (2006). Tidal circulation and energy dissipation in a shallow, sinuous estuary. *Ocean Dynamics*, *56*(3–4), 360–375.

Seim, H. E., & Gregg, M. C. (1997). The importance of aspiration and channel curvature in producing strong vertical mixing over a sill. *Journal of Geophysical Research*, *102*(C2), 3451–3472.

Seminara, G. (2006). Meanders. *Journal of Fluid Mechanics*, *554*, 271–297.

Shapiro, A. H., & Sonin, A. A. (2018). Advanced fluid mechanics problems. Self-published manuscript.

Shchepetkin, A. F., & McWilliams, J. C. (2005). The regional oceanic modeling system (ROMS): A split-explicit, free-surface, topography-following-coordinate oceanic model. *Ocean Modelling*, *9*(4), 347–404.

Signell, R. P., & Geyer, W. R. (1991). Transient eddy formation around headlands. *Journal of Geophysical Research*, *96*(C2), 2561–2575.

Smith, R. (1982). Where to put a steady discharge in a river. *Journal of Fluid Mechanics*, *115*, 1–11.

Thackston, E. L., & Schnelle, K. B. (1970). Predicting effects of dead zones on stream mixing. *Journal of the Sanitary Engineering Division*, *96*(2), 319–331.

Thomson, J. (1877). V. on the origin of windings of rivers in alluvial plains, with remarks on the flow of water round bends in pipes. *Proceedings of the Royal Society of London*, *25*(171–178), 5–8.

Umlauf, L., & Burchard, H. (2003). A generic length-scale equation for geophysical turbulence models. *Journal of Marine Research*, *61*(2), 235–265.

Warner, J. C., Armstrong, B., He, R., & Zambon, J. B. (2010). Development of a coupled ocean–atmosphere–wave–sediment transport (COAWST) modeling system. *Ocean Modelling*, *35*(3), 230–244.

Warner, S. J., & MacCready, P. (2014). The dynamics of pressure and form drag on a sloping headland: Internal waves versus eddies. *Journal of Geophysical Research: Oceans*, *119*, 1554–1571. https://doi.org/10.1002/2013JC009757

Warner, J. C., Sherwood, C. R., Arango, H. G., & Signell, R. P. (2005). Performance of four turbulence closure models implemented using a generic length scale method. *Ocean Modelling*, *8*(1–2), 81–113.

Wolanski, E., Imberger, J., & Heron, M. L. (1984). Island wakes in shallow coastal waters. *Journal of Geophysical Research*, *89*(C6), 10,553–10,569.

Zhong, L., & Li, M. (2006). Tidal energy fluxes and dissipation in the Chesapeake Bay. *Continental Shelf Research*, *26*(6), 752–770.